Geological analysis of Martian rover-derived Digital Outcrop Models using the 3D visualisation tool, Planetary Robotics 3D Viewer – PRo3D.

Robert Barnes[1], Sanjeev Gupta[1], Christoph Traxler[2], Thomas Ortner[2], Arnold Bauer[3], Gerd Hesina[2], Gerhard Paar[3], Ben Huber[3]†, Kathrin Juhart[3], Laura Fritz[2], Bernhard Nauschnegg[3], Jan-Peter Muller[4], Yu Tao[4].

[1]Department of Earth Science and Engineering, Imperial College London, London, SW7 2AZ, UK.

[2]VRVis Zentrum für Virtual Reality und Visualisierung Forschungs-GmbH, Donau-City-Strasse 11, 1220, Vienna, Austria.

[3]Joanneum Research, Steyregasse 17, 8010, Graz, Austria.

[4]Mullard Space Science Laboratory, University College London, Holmbury Hill Rd, Dorking RH5 6NT, UK.

†Presently at ETH Zürich.

Corresponding author: Robert Barnes (robert.barnes@imperial.ac.uk)

Key Points:

- Processing of images from stereo-cameras on Mars rovers produces 3D Digital Outcrop Models (DOMs) which are rendered and analysed in PRo3D.

- PRo3D enables efficient, real-time rendering and geological analysis of the DOMs, allowing extraction of large amounts of quantitative data.

- Methodologies for sedimentological and structural DOM analyses in PRo3D are presented at fou-r localities along the MSL and MER traverses.

Abstract

Panoramic camera systems on robots exploring the surface of Mars are used to collect images of terrain and rock outcrops which they encounter along their traverse. Image mosaics from these cameras are essential in mapping the surface geology and selecting locations for analysis by other instruments on the rover's payload. 2D images do not truly portray the depth of field of features within an image, nor their 3D geometry. This paper describes a new 3D visualization software tool for geological analysis of Martian rover-derived Digital Outcrop Models (DOMs) created using photogrammetric processing of stereo-images using the Planetary Robotics Vision Processing (ProViP) tool developed for 3D vision processing of ExoMars PanCam and Mars 2020 Mastcam-Z data. DOMs are rendered in real time in the Planetary Robotics 3D Viewer PRo3D, allowing scientists to roam outcrops as in a terrestrial field campaign. Digitisation of point, line and polyline features is used for measuring the physical dimensions of geological features, and communicating interpretations. Dip and strike of bedding and fractures is measured by digitising a polyline along the contact or fracture trace, through which a best fit plane is plotted. The attitude of this plane is calculated in the software. Here, we apply these tools to analysis of sedimentary rock outcrops and quantification of the geometry of fracture systems encountered by the science teams of NASA's Mars Exploration Rover *Opportunity* and Mars Science Laboratory rover *Curiosity*. We show the benefits PRo3D allows for visualisation and collection of geological interpretations and analyses from rover-derived stereo-images.

Plain Language Summary

Key data returned from robots exploring the surface of Mars are the images they take of the landscape and rock formations. These are sent back to Earth for detailed investigation and analysis by the science teams. It is difficult to collect reliable measurements from photographs, as they do not truly represent the three-dimensionality of the features within them. In this paper, we present a new 3D visualisation software tool, PRo3D, which enables visualisation of 3D digital models of rock outcrops imaged by robots exploring the surface of Mars. These 3D models are constructed from mosaiced photographs taken by the stereo panoramic cameras which are positioned on a mast on the rover. This provides a huge advantage to scientists who want to study and analyse the terrain and geology of exposed rock outcrops which surround the rover. Here we apply the tools available in PRo3D to sedimentological and structural analysis of 3D Digital Outcrop Models (DOMs) of four areas explored by the Mars Exploration Rover *Opportunity* and Mars Science Laboratory *Curiosity*

rover science teams, and show that this method of 3D visualisation and analysis allows scientists to carry out important procedures that would be conducted in a terrestrial field geology campaign.

1. Introduction

One of the principle objectives for past and current rover missions to Mars has been to characterise the geology of sedimentary rocks exposed at the Martian surface to identify evidence for long lasting water activity and the existence of habitable environments at some point in the planet's history (Arvidson 2016; Arvidson *et al.*, 2011; 2014, 2016; Clark *et al.*, 2016; Edgar *et al.*, 2014, 2017; Grotzinger *et al.*, 2005, 2006; 2012; 2014, 2015; Crumpler *et al.*, 2011, 2015; Metz *et al.*, 2009; Siebach *et al.*, 2014; Vaniman et al., 2014; Squyres et al., 2004, 2008; Ruff et al., 2011; Vasavada et al., 2015; Stack *et al.*, 2016; Rice *et al.*, 2017). The primary instruments used to make these observations, and place observations from other instruments in their correct context, are the rover's cameras. Engineering cameras (Navigation Cameras – Navcams – on the rover mast, and Hazard Avoidance Cameras – Hazcams – at the front and rear) are used for localisation and navigation, as well as target selection and drive planning (Arvidson *et al.*, 2003; Alexander *et al.*, 2006; Tao & Muller 2016b). Science cameras are generally of a higher resolution, and are situated on rover masts or arms, and allow for acquisition of detailed imagery of specific areas and targets selected from the Navcam imagery. Intuitive software tools to quantitatively characterise geological observations using scaled 3D reconstructions of rover images, are therefore essential to efficient analysis and decision making.

The Navcam, Pancam and Mastcam instruments, carried as payloads on NASA's Mars Exploration Rover (MER) and Mars Science Laboratory (MSL) missions, as well as the PanCam on ESA's ExoMars 2020 Rover and Mastcam-Z on NASA's Mars2020 Rover are stereo-cameras, allowing for reconstruction of the rover's environment in three-dimensions. Tools for analysis of reconstructed 3D stereo rover imagery have been developed in MATLAB® for scientific analysis (Lewis *et al.*, 2008; Hayes *et al.*, 2011; Edgar *et al.*, 2012, 2017) and the Multimission Image Processing Laboratory (MIPL) tool was used by the MER and MSL science teams for traverse planning and contact science algorithm development (Alexander *et al.*, 2006). Other science planning tools are used by science and instrument teams for different missions such as Maestro for MER (NASA 2015), PSI for Phoenix (Fox

and McCurdy 2007), and MSLICE for MSL (NASA/JPL 2015) to plan observations and write commands.

There is, however, a need for specific tools which are user-friendly and allow a wide-range of scientists to quantitatively analyse 3D reconstructions of stereo-images. Such a 3D environment allows for application of approaches developed in terrestrial field geology; observing and analysing the mineralogical, geometrical and dimensional variations of rock outcrops. Outcrops in the field are characterised through systematic observation of the rock types, grain size, sorting and angularity, layer thickness, nature of the boundaries between layers, thickness of geological units, their geometrical relationships, and the geometry and dimensions of sedimentary structures formed as a result of the processes by which the sediments were deposited.

Recent advances in 3D Digital Outcrop Model (DOM) data collection, visualisation and tool development have greatly improved analysis techniques and understanding of terrestrial datasets (Verwer *et al*., 2004; Pringle *et al*., 2006, 2013; Enge *et al*., 2007; Viseur *et al.,* 2007*;* Buckley *et al.,* 2006, 2008a, 2008b; Adams *et al.,* 2009; Fabuel-Perez *et al*., 2009; van Lanen *et al.,* 2009; van Lanen 2010; Hodgetts 2013; Rarity *et al*., 2013; Sahoo & Gani 2015). These studies rely on multiple datasets derived from LiDAR scanning, photogrammetry, digital photography, as well as field collected data, and are typically used to populate statistical models to assist in hydrocarbon and mineral exploration. Improvements in the data quality and processing techniques from Mars rover imaging systems enable high quality 3D point cloud models of outcrops on Mars, to which these field scale studies can be applied.

Key requirements of 3D data visualisation and analysis software for Martian rover-derived DOMs are to; (i) efficiently select and visualise the desired data from multiple rover localities enabling the user to view multiple datasets in a single environment; (ii) roam the outcrop to view features of interest from different positions; (iii) highlight and communicate the locations of Regions of Interest (ROIs) for collaborative investigation; (iv) annotate and interpret geological features and boundaries directly onto the 3D reconstruction; (v) perform repeatable measurements of feature dimensions (e.g. grain size, layer thickness) and geometries (e.g. strike and dip). The Planetary Robotic 3D Viewer (PRo3D) has been designed for this purpose as part of the EU-FP7 Planetary Robotics Vision Data Exploitation (PRoViDE) project (Paar *et al*., 2015; Traxler *et al*., 2018), enabling users to roam and analyse mm to cm scale digital reconstructions of the terrains encountered and imaged by

Martian rover missions, which have been reconstructed using the Planetary Robotics Vision Processing tool, PRoViP; an automated processing chain incorporating feature matching and 3D reconstruction algorithms.

In this paper, we describe the input data, outline the processing in PRoViP to create the 3D DOMs, how they are rendered in the software, as well as their limitations in geometry and resolution. The methods for obtaining a detailed understanding of the geology of Mars are outlined, followed by a description of how these methods are enabled by tools within PRo3D. We have selected four case studies to test these applications: three locations along the MSL traverse and one in Victoria crater, visited by the MER *Opportunity* rover. These allow us to test various workflows for sedimentological and structural analysis, as well as compare our results to those from previous work. In this paper, we show the capabilities of a 3D environment like that provided by PRo3D for extracting quantitative information from rover-derived stereo images.

2. PRo3D Viewer

2.1. Input data

2.1.1. Camera properties

Mars Exploration Rover camera systems

The MER left and right Pancam CCD sensors return images up to 1024 x 1024 pixels in size with a 16º x 16º field-of-view (FOV), allowing for an Instantaneous-Field-of-View of 28 mrad/pixel (Bell *et al*., 2006). They are mounted to the Pancam Mast Assembly (PMA) with a fixed-baseline stereo separation of 30 cm and are 1.5 m above the base of the wheels. Each sensor has a filter wheel allowing for imaging in 11 different wavelengths, ranging from 432 to 1009 nm with bandpasses from 16 to 38 nm (Bell *et al*., 2006). The two MER Navcam CCD sensors are situated between the Pancam sensors on the PMA, with a separation of 20 cm. They each have a 1024 x 1024 detector capable of a 45º field of view, which can generate images of 0.82 mrad/pixel at the centre of the field of view (Maki *et al*., 2003).

Mars Science Laboratory Curiosity Rover camera systems

The Mastcam sensor is comprised of two multispectral digital cameras situated on the rover's mast, 1.97 m above the base of the wheels (assuming it is on a flat surface). On the right (with respect to the rover) is the M-100 camera, 100 mm focal length 1600 x 1200 pixel CCD sensor with an f/10 lens and 6.8º x 5.1º FOV. This yields an IFOV of 0.074 mrad/pixel (Malin *et al*., 2017). 24.2 cm to the left of the M-100 sensor is a 34 mm focal length (M-34) CCD sensor with an f/8 lens with a FOV of 20º x 15º, allowing it to obtain images with an IFOV of 0.22 mrad/pixel at a scale of 450 microns per pixel at a range of 2 m, and 22cm per pixel at 1 km (Malin *et al*., 2017). Radiometric and geometric calibration of these cameras allows for high quality geological analysis, and stereo-reconstruction (Bell *et al*., 2017).

The MSL Navcam system consists of four digital cameras attached to the same camera plate as the Mastcam instrument. One pair of these is active at a time. Each Navcam has a 45-degree square field of view, and an IFOV of 0.82 mrad/pixel (Maki *et al*., 2012).

The navigation and science cameras are connected to the mast via a Pan-Tilt Unit (PTU). This allows the camera to tilt and rotate about the PTU axis, allowing for the collection of tiled panoramas. The size of these panoramas, and whether they are stereo or not is determined primarily by science rationale, as well as the rover's internal storage, bandwidth limitations, time, and power constraints during rover planning.

2.1.2.   *Data processing*

The PRoViP tool was developed as part of the PRoVisG (Paar *et al*., 2012) and PRoViDE (Paar *et al*., 2015) projects by Joanneum Research. ProViP integrates a variety of 3D vision algorithms in modular processing chains, which are used to create panoramas and Digital Terrain Models (DTMs) in Ordered Point Cloud (OPC) format which can be rendered in PRo3D. The OPCs incorporate the image data, and camera poses as determined from SPICE data. The individual products are stored in a database (PRoDB) and SQL queries are used to identify and select relevant data for processing. Specific data structures ensure efficient visualization and support the modelling of the DTM fitting best to the geometric peculiarities of the sensor space.

Effectively the same techniques are used for processing of the MER Pancam and MER and MSL Navcam imagery, but the MSL Mastcam provides additional challenges for processing. The different focal lengths of the M-100 and M-34 cameras result in the M-100 sensor effectively imaging at 3x magnification compared to the M-34 camera. To overcome

this disparity in image resolution of the two cameras, pre-registration of the M-34 images with their M-100 counterpart is carried out to upscale it prior to stereo-reconstruction and mosaicking. Lateral resolution is determined by the CCD sensor size (Bell *et al*., 2006) and the distance of the imaged object from the CCD sensor. Resolution drops quadratically with distance.

2.1.3. Data limitations

Errors in stereo-camera alignment and stereo-matching used to create the 3D scene result in data points plotting at erroneous distances from the true surface, resulting in an irregular surface which increases in roughness with distance from the sensor. Distortion of the OPCs can be induced by variations in temperature during image capture, and errors in the determination of camera poses. OPCs are commonly best viewed from the location the image was taken from, and show increasing co-registration artefacts when the view is rotated (Supplementary Information, Fig. S1a – b). This effect is variable across the traverses to date, due to differing proximity of the imaging equipment to the outcrop and number of stereo pairs taken. Due to precise knowledge about imaging geometry, however, the expected error is always known.

Different lighting conditions presently reduce the capability of obtaining large consistent OPCs from multiple locations. Individual OPCs can, however, be combined in PRo3D to reduce the impact of this issue. The difficulty of locating the position of the rover during image capture to within a few metres, together with orbital DTM spatial resolution no greater than 1 m, results in shifts of OPC positions in relation to each other (Supplementary Information, Fig. S1c – d), though they can be manually moved in the viewer to ensure a closer fit. In the spatial domain, an automated coregistration method (Tao & Muller, 2016b) has been applied to orbiter and rover orthorectified images to refine rover poses (position & pointing). The spatial positioning errors of rover images are therefore minimized to sub-pixel level of HiRISE orthorectified images, which are co-registered with Context Camera (CTX on NASA's Mars Reconnaissance Orbiter - MRO) and High Resolution Stereo-camera (HRSC on ESA's Mars Express) data.

Areas in occlusion from the camera systems, such as those behind boulders, around corners and beneath overhangs cannot be imaged, and this can result in holes in the data, or stretched regions (Supplementary Information, Fig. S1e – f).

2.2. 3D rendering and digitisation in PRo3D

Stereo-reconstructed imagery is converted to OPC format for analysis in PRo3D. This data structure was designed to represent the terrain in multi-resolution and from multiple sources, using Level of Detail (LoD) visualisation. LoD visualisation ensures that the appropriate geometric resolution is chosen for real-time visualisation depending on the screen resolution, the distance to the viewpoint and the angular resolution of the source data given, thus resulting in visualisation of high-resolution textures and surfaces at close distances to the OPC and low resolution at larger distances. LoD changes incrementally, and these increments can be specified by the user.

Texture descriptions embedded in the OPC contain: the actual image data (RGB values), the texture coordinates (image pixel locations) for mapping the image onto the patch, and a validity/weights image that encodes valid and invalid regions of the image part. An invisible surface from which measurements are taken – the k-d-tree – is generated at the highest Level of Detail and saved as a cache file. Care must be taken during interpretation to select appropriate parts of the OPC for measurement, and results should be visually checked during the interpretation process. The navigation and layer selection tools in PRo3D allow for this to be a straightforward action.

3. Essential geological tools for reconstructing ancient depositional processes and environments on Mars

3.1. Geological mapping using photomosaic interpretation

On Earth, geological maps are prepared in the field by plotting the locations of rock outcrops, identifying their lithology and taking structural measurements to determine the relative age relationships of the rocks exposed there. Geological contacts are plotted based on these observations, and extended into areas of no outcrop based on the relationship between the inclination (dip and strike) of the bedding, and surface topography, as well as changes in weathering, vegetation, and soil character. Aerial photographs and satellite imagery are also commonly used to create geological maps, particularly in arid and inaccessible areas. Geological mapping of Mars presently relies mostly on orbital images using techniques summarised by Beyer *et al*., (2015). The resultant geological map is highly dependent on the resolution of the images, which are between 0.25 and 250 m (Beyer *et al.,* 2015) and the scale at which the map was constructed.

Observations from the MER and MSL rover missions have revolutionized our understanding of the geology of Mars. The far higher resolution of data collected from the surface allows for greatly improved process-based interpretations of the geology (Grotzinger *et al*., 2005; Lewis *et al*., 2008; Metz *et al*., 2009; Crumpler *et al*., 2015; Stack *et al*., 2016). It is also possible that the images returned from these rover missions may be the only images of those locations ever taken, so far more care and attention is placed on interpreting as many details as possible from each outcrop than may be taken during terrestrial field campaigns. A limitation of this approach lies in the current lack of well-developed, widely available tools specifically created for visualisation of rover-derived surface imagery. PRo3D has been developed to carry out this task in a 3D environment, which allows stereo-images taken on different sols and locations to be spatially related and analysed, providing a greater contextual framework for interpretation. It is also possible to extract a large amount of repeatable measurements directly within the viewer in a relatively short space of time. A summary diagram of the interpretation tools in PRo3D is shown in Figure 1a.

3.2. Distance measurement

The scale and dimensions of geological features provide essential information to fully characterise the geology and aid interpretation of palaeoenvironments. Simple point to point distances for scale, unit and bed/lamination outcrop thickness, set thickness, width of discontinuous units and bedding, as well as grain size are the primary values to measure. Estimates of the dimensions of imaged features of interest can be made directly from an image when the IFOV and the distance from the sensor to the object are known. If the viewpoint is not orthogonal to the imaged surface, the scale of each pixel is highly variable throughout the image. 3D stereo-reconstruction of mosaics from Martian rover camera systems is therefore essential in obtaining accurate measurements of rock outcrops.

3.3. Geometrical analysis of geological features

Geological surfaces, such as laminations, bedding surfaces, and fractures are, at some scale, planar. A plane can be uniquely described by the orientation of the direction of maximum dip, which is perpendicular to an imaginary horizontal line on that surface (the strike), and the magnitude of that dip. Therefore, dip and strike measurements are essential for determination of structural and geometric relationships between geological units and bedding and fractures within, thus allowing for identification of unconformities and structures related to sedimentation, deformation and diagenesis. Geometrical analysis of cross-stratification permits reconstruction of palaeoflow directions (Dott, 1973; High and Picard,

1974; Michelson and Dott, 1973; Lewis *et al*., 2008; Hayes *et al*., 2011; Edgar *et al*., 2012), thereby assisting in determination of palaeodrainage patterns and sediment routing systems. Collection of dip and strike data also enables conversion of apparent thicknesses of dipping stratigraphic sections measured on the outcrop to true thicknesses; a vital functionality for construction of stratigraphic logs. Incorporation of palaeocurrent directions into channel and dune width and thickness measurements on the outcrop also enable the determination of the true dimensions of these sedimentary features (van Lanen *et al*., 2009), as well as a more reliable indication of their large-scale geometries.

4. Geological measurement tools in PRo3D

4.1. Distance measurement

Simple 3D straight-line distances can be calculated using the line tool. This involves picking two points on the surface and the shortest distance between the start and end point of each line is automatically calculated, as well as the distance parallel to the Up Vector, the bearing, and slope of the line. Polylines can also be set to project the lines between each vertex in this manner. The three-dimensional distance along a surface can be determined by either orthographic or viewpoint projection of the line between the start and end points which intersects the OPC surface. Orthographic projection involves vertically projecting the 3D line between the constituent points flush against the outcrop, and viewpoint projection (Fig. 1) involves projecting the intermediate lines in a plane parallel to the view pitch and bearing. This can also be useful for visualisation of the weathering profile of a DOM.

4.2. Interpretation and annotation of the OPC

Detailed interpretations can be digitised directly onto the OPC surface in PRo3D, allowing for visual representation of the spatial distribution of geological units, and important features. This is useful for subsequent measurement and analysis as well as communication of interpretations within the planetary geoscience community.

Two types of lines can be digitised: two-point lines, which are useful for measuring distances and heights, and multipoint polylines, which are useful for delineating features and boundaries. Line thickness and colour can be modified before and after polylines have been completed, using a standard point weight system for thickness and red, green and blue (RGB) spectrum for the colours. This allows for development of a simple line symbology, which can be used to specify various types of boundaries (Fig. 1a). Point digitisation allows for

extraction of the xyz coordinates at those points, and all digitised features can be annotated in 3D space.

Bookmarks can also be created, which allow the user to save a viewpoint, and summon it with one click.

4.3. Measurement of bedding and structural feature orientations

Dip and strike measurements provide a unique, quantitative measure of the three-dimensional orientation of bedding and structural features. A tool was developed within PRo3D to determine dip and strike values directly from the OPC surfaces in DOMs. Points are digitised along well defined planar sections of sedimentary and structural contacts which possess sufficient surface topography. The xyz coordinates of these points are obtained and a best fit plane through the digitised points is calculated, using the method of least squares regression, taking a comparable approach to that employed by Kneissl *et* al., (2010). A series of vector and trigonometrical calculations are carried out on the resultant plane (summarised in Supplementary Information Fig. S2) to compute the dip and strike with respect to north and horizontal. These data are recorded within the software, and the values can be exported as .csv files allowing for further statistical analysis.

Dip and strike values are presented in PRo3D as vectors in 3D space, at the central point of the digitised sequence of points (Fig. 1). The best fit plane can be visualised, and is coloured according to the dip magnitude (red = high, blue = low). The intersection of these planes with the OPC surface can be viewed to allow for a first-pass quality control assessment of the dip and strike calculation – if the intersection follows the mapped contact, the dip and strike of the best fit plane is like a reasonable value. Strike measurements are the bearing of a unique horizontal line on a plane, and are described as bearings relative to magnetic north. Map projections ensure that field measurements should be corrected to grid north. Dip measurements are taken relative to the direction of acceleration of local gravity – or down, and can also be easily measured in the field on Earth, with values relative to the orientation of the geoid surface. Digital analysis of outcrops is not conducted in an environment in which these laws of nature occur; the directions of north and up must be specified within the software. The local up or down (surface normal) vector is calculated between the planetary centre, and the centre of rotation of an OPC surface in the viewer. The direction of north is calculated from this vector.

5. PRo3D geological analysis workflow

5.1. Introduction

Four localities visited by the MER and MSL missions were selected as case studies to test the application of PRo3D and the incorporated geological analysis tools; Yellowknife Bay (Fig. 2a), visited by the MSL rover *Curiosity* between Sols 54 – 330, Bridger Basin, which was visited between sols 1082 and 1110 by *Curiosity* (Fig. 2b), Garden City (Fig. 2c) also visited by *Curiosity* during sols 918 – 926 and Victoria crater, visited by the MER rover *Opportunity* between sols 952 and 1634 (Fig. 2d). This section presents some examples of the geological analyses which are possible in PRo3D. All analyses follow the relevant steps of a workflow comparable to that used for field investigation of outcrops (Supplementary Information, Fig. S3). This involves first exploring the outcrop, then identifying individual units and their boundaries, before taking relevant measurements and making textural observations.

5.2. Geological investigation of the Yellowknife Bay area

In order to demonstrate how PRo3D can be used to understand the stratigraphic and structural relationships of a geological interesting area area, we carried out a detailed investigation of the rocks exposed at Yellowknife Bay (YKB) (Fig. 2a). The YKB area was visited by the MSL *Curiosity* rover shortly after it landed in Gale crater, between Sols 54 and 330 of operations (Grotzinger *et al*, 2014; Vasavada *et al*., 2014). Following descent to the lowest exposed unit at YKB, the MSL science team characterised the stratigraphy of layered strata in this area. These strata were assigned to the Yellowknife Bay formation, which was further sub-divided into three members in ascending stratigraphic order; the Sheepbed member, the Gillespie Lake member, and the Glenelg member. These are primarily detrital rocks of basaltic bulk composition, and are interpreted as the deposits of distal fluvial fan and lake palaeoenvironments (Grotzinger *et al*., 2014). For our analysis, a DOM of YKB was created by combining multiple Mastcam, Navcam and super-resolution restored (SRR) HiRISE (Tao & Muller 2016a) OPCs. Navcam datasets were manually translated to fit best with features identified in the SRR HiRISE, and the Mastcam data was translated, where necessary to match features in both the Navcam and other Mastcam OPCs. The resulting DOM was interpreted following relevant parts of the outcrop interpretation workflow (Supplementary Information, Fig. S2), and is shown in Figure 3.

The basal strata form the Sheepbed member mudstone, characterised by sub-horizontal layering and decameter scale polygonal fracturing (Grotzinger *et al*., 2014;

Schieber *et al*., 2017), as well as distinctive diagenetic features such as nodular concretions (Stack *et al*., 2014), veins, raised ridges and possible synaeresis cracks (Siebach *et al*., 2014). The Gillespie member sandstone overlies the Sheepbed mudstones and is a medium-grained sandstone (Grotzinger *et al*., 2014), which is more resistant to weathering than the Sheepbed, forming protrusions and overhangs. It is also polygonally fractured, but shows a blockier character than the Sheepbed member. The Glenelg member is more sedimentologically variable than the underlying units, and has been mostly characterised at the rough-textured, vuggy, with poorly preserved laminations Point Lake outcrop (Grotzinger *et al*., 2014), and the cross-stratified, medium- to coarse-grained sandstone Shaler outcrop (Edgar *et al*., 2017) (Fig. 3a). The overall stratigraphy shows a general coarsening upwards succession.

The area covered by the combined OPCs in this study is 30 m across, and a ~14 m wide area of this was investigated in detail in PRo3D. Mapped features in Figure 3 have been interpreted from the Mastcam OPCs, and show a good alignment with the features visible in the HiRISE image. Key targets and features of interest have been labelled in PRo3D to highlight their scale and locations in relation to each other. Annotated features include: the John Klein and Cumberland drill holes, a curvilinear clastic dyke referred to as "The Snake" (Grotzinger *et al*., 2014), an area of the Sheepbed member brushed by the rover's Dust Removal Tool (DRT), and the Gillespie anticline.

White lines were used to mark layer contacts in the Sheepbed member (Fig. 3), and these indicate considerable variability in layer thickness within the member. A particularly striking example of this is shown in Fig 5d, where the thickness of an individual mapped layer of the Sheepbed decreases from 36 cm in the left, to 8 cm where the contact is obscured due to occlusion, but is inferred to be truncated by the Sheepbed-Gillespie contact. This contact dips shallowly to the east, dips up to 7° to 080°, and shallows out where it is thickest to 5° to 057°. Mapped concentrations of nodular concretions show irregular boundaries between areas populated by concretions and those in which they are absent. The boundaries are in some places consistent with internal layer contacts within the Sheepbed member, and in some places they cross-cut contacts.

The red line in Figure 3a is the Sheepbed-Gillespie boundary, which is highly irregular, and abrupt, with an overall dip of 1° - 4° to the southeast (metre scale dip measurements in Fig. 3b) . The irregular morphology of the Sheepbed-Gillespie Lake boundary is a result of localised scours commonly between 1 and 2 m wide, and 2 – 20 cm deep. A particularly well-preserved example of such a scour is shown in Figure. 4a. One of

the scours has a width of 5 m, and measurements in PRo3D show that up to 43 cm of the Sheepbed member was eroded (Fig. 4b). Dip and strike measurements (N=10) along the scours favour a northwesterly orientation (Fig. 4a), which may be interpreted as a proxy for the flow axis during deposition.

The light blue boundary in Fig 3a outlines the outcropping part of 'The Snake'(Grotzinger *et al*., 2014), which has an outcrop length of 11.7 m. It outcrops from the Sheepbed-Gillespie contact, trending to 065° and shows a 90° kink approximately 9 m northeast of that boundary. Where it trends NE-SW, it has a width around 13 cm, which increases to 25-30 cm at the kink. The Gillespie anticline (Figs. 3a & 4c) is an up to 6.8 m wide fold, which has a maximum amplitude (measured at the Sheepbed-Gillespie boundary) of 54 cm. The dips and strikes measured from this structure have been plotted as poles to planes in a stereonet (inset, Fig. 4), which can be used to define the fold as a gentle (142° interlimb angle), upright fold, with a fold axis striking to 242° (NE-SW), which is approximately perpendicular to the trend of the Snake. Limb dips are commonly lower than 10° but reaching a common maximum of 19°. The fold has a slight asymmetry and vergence to 154° (plunging 4°). This requires around 20 cm of shortening. The Gillespie anticline can be interpreted as a result of rapid accumulation of the Gillespie Lake sandstone member over a poorly lithified substrate, with deposition occuring in a southeasterly direction. This accumulations resulted in differential compaction and dewatering forming the low angle anticline, with a direction of shortening parallel to the inferred palaeoflow direction.

These results from PRo3D at YKB build on previously published work (e.g. Grotzinger *et al*., 2014; Schieber *et al*., 2017), allowing us to characterise layer geometries in the Sheepbed member, which, when visualised in PRo3D, show extra complexity, possibly a a result of palaeotopograhy, or due to syn-sedimentary deformation. Downcutting of the Gillespie Lake member has formed two populations of scour geometries; up to 1 m wide scours, and larger, up to 7 m wide features, superimposed by smaller scours (2 – 20 cm deep). Dip and strike measurements imply that flow was along a NW-SE axis. The geometry of the Gillespie anticline has been described quantitatively, showing that it shortened to the southeast, as has its geometrical relationship to the Snake, which is sub-parallel to the calculated fold axis. This observation together with the spatial relationships imply that the structures are related, and are the surface expression of syn-sedimentary deformation during Gillespie Lake member accumulation.

5.3. Reconstruction of sedimentary architecture in the Stimson formation at the Williams outcrop

To characterise the detailed 3D architecture of cross-stratified sandstones in the Stimson formation, we used PRo3D to map sedimentary structures and analyse the relationship between key sedimentary elements in the outcrop, such as foresets and set bounding surfaces, and to determine bedset thicknesses and their variability. The Stimson formation is a several 10s of metres thick, well-sorted, fine to medium sandstone containing abundant sets of cross-laminations up to 1 m thick (Banham *et al*., 2018). This unit has been interpreted as an aeolian deposit that unconformably overlies the lacustrine Murray formation (Banham *et al*., 2018). The Williams outcrop is the best example of preserved simple aeolian dunes imaged by *Curiosity* within the Stimson, and occurs on the NW face of an approximately NE-SW trending ridge known as the Bob Marshall ridge (Fig. 2b). The outcrop is up to 4.6 m high, and a 14 m wide area was analysed here. It was photographed when the rover mast was approximately 2 m from the base of the outcrop, which slopes at 15° – 20° to a distance of about 13 m. Detailed analysis of Williams outcrop was undertaken using a DOM derived from OPCs created using stereo mosaics collected on Sols 1087, 1090 and 1092 (Fig. 5) to determine foreset dip-azimuth and cross-set thickness, as well as to understand the geometrical relationships between the foresets and their underlying bounding surfaces. The 6 bedsets identified by Banham *et al*., (2018) were mapped onto the DOM. Cross-lamination orientations were estimated using the dip and strike tool in PRo3D (subset shown in Fig. 5). These were determined set-by-set and organised into groups and this data was then extracted and plotted in the Orient software (Vollmer *et al*., 1995; Vollmer 2015), with all sets grouped together, as well as in individual sets to ascertain variability up section (Fig. 5). The data is summarised in Table 1. The foreset dip azimuth directions recorded from the Williams outcrop are discussed in detail, along with the sedimentology of the Stimson formation by Banham *et al*., (2018). Overall dip directions show a vector mean dune palaeotransport of 059°, with a vector magnitude of 0.85 ("All cross-laminations", Fig. 5a, Supplementary Information Table S1). All the set boundary dips and strikes (inset stereonet Fig. 5a) are 2° – 14° to the NW (062°, N = 15). The foresets show asymptotic geometries which are evidenced clearly in Coset 2a (Fig. 5b), by both the curved expression of the digitised lamination contacts, and by the change in colour of the dip and strike disks (red at the top of the set, yellow-orange in the middle, and green at the base – disks are coloured by dip value). Maximum dip values of up to 37° were calculated at the top of the set in fig 7b,

with 10°-12° measured in the middle, and the minimum observed values of 4° were found at the base of the set (Fig. 5b). Laminations in each set show a wide range of strike values (Fig. 5c), which, together with the information on set boundary and and foreset geometry presented here, indicates that the structures exposed at the Williams outcrop are troughs which are exposed in profile.

Here we show the benefits that PRo3D offers in reconstructing the detailed geometry of these cross sets. Feature grouping and data export functionalities allow us to dissect the data set by set, and compare the palaeoflow directions recorded with the underlying basal surface orientation of each set, in order to determine the three-dimensional sedimentary architecture and understand the kinematics of the sedimentary structures present. Following comparable methodologies to those described in DeCelles *et al.*, (1983) and Almeida *et al.*, (2016), dip and strike values of the palaeocurrent measurements in each set were plotted in a stereonet, together with the basal surface dip and strike values measured. The Bingham axial distribution of the poles of individual measurements in each population was calculated in the Stereonet software (Allmendinger *et al.*, 2013; Cardozo *et al.*, 2013), and the plane that is described by the maximum eigenvector for each population was plotted. This allows us to visualise the relationship between recorded dip azimuths, and surface geometry. Plotting the intersection of these two mean planes gives the relationship between them. This is a purely geometric measure which does not take kinematics into account, but predicts that where the laminations dip oblique to the underlying surface, the intersection line between them will climb or descend the basal surface at an angle determined by the obliquity. The results are summarised in Supplementary Information Table S1 and plotted in lower hemisphere equal angle stereonets in Figure 5c.

All set lamination dip directions were oblique to the strike of the underlying basal surfaces (Fig. 5c), apart from Set 4, in which the laminations dipped only slightly oblique to the basal surface dip direction, indicating that it was travelling down the surface. The observed direction of intersection migration was markedly different to the vector mean of the cross-lamination dip directions measured, with the exception of sets 2 and 3, varying from a climb of 4° to 116° in Set 1, to climbs between -2° - 7° to a bearing between 071° and 091° in sets 2 – 4. Set 5 is comparable to Set 1 in that the migration is 10° to 104°.

Set thickness measurements were also taken at 10–20 cm intervals along each individual set, by drawing a line from the base to the top whilst viewing approximately perpendicular to the dominant palaeflow direction as determined by the lamination dip and strike values (Fig. 6a). The vertical distance from the start point to the end point of each line was recorded. These values were not corrected for the dip and strike of the set boundaries as they are not parallel, and the effect would be negligible in this case. The values were plotted in histograms to determine the variability (Fig. 6b). Set 1 varies in thickness from 0.17 - 0.38 m, and most values are between 0.17 and 0.2 m. Coset 2 ranges from 0.69 – 0.97 m in thickness, with most values falling between 0.88 and 0.97 m. Set 3 is 0.45 to 1 m thick and shows peaks around 0.61 and 0.96 m. Set 4 is 0.33 – 0.82 m thick and most values are between 0.36 and 0.54 m thick. The tapering geometry of set 5 is reflected in the high range of values (0.21 – 1.08 m), with most values in the lower thickness range of 0.2 – 0.3 m.

These results gained from the 3D DOM highlight the true complexity of the dune depositional architectures in the Stimson formation, which would either be very time consuming, or not possible from 2D mosaic interpretation. We show that dune migration occurred by overall NE movement of dunes over bounding surfaces dipping to the NW. This obliquity caused the dunes which formed sets 1, 2, 3, and 5 to migrate up the basal surface in a NE to SE direction, further evidence in support of the aeolian interpretation by Banham *et al.*, (2018). Application of the roaming capabilities of PRo3D, together with the palaeomigration directions calculated from the cross laminations allowed us to ascertain true thickness valused for the sets which form the outcrop, as well as to assess their variability.

5.4. Fracture analysis at Garden City

The *Curiosity* rover science team has encountered many prominent diagenetic features in the form of nodules, raised ridges, dendritic/lenticular crystals and veins or mineral filled fractures in almost all stratigraphic units encountered by the rover (Blaney *et al.,* 2014; Grotzinger *et al.*, 2014, 2015; Leveille *et al.*, 2014; Nachon *et al.*, 2014, 2017; Siebach *et al.*, 2014; Stack *et al.*, 2014; Kah *et al.*, 2015; Mangold *et al.*, 2015; Kronyak *et al.*, 2015; Van Bommel *et al.*, 2016; Schieber et al., 2017; Young & Chan 2017). One of the most striking examples of these features was a vein network observed at the Garden City target (see Fig. 2c for location). These veins are interpreted to have formed by precipitation of minerals from saturated brines which have circulated through the fractures (Nachon *et al.*, 2014, 2017). Three generations of vein-fill are identified based on colour and textural variations; one

forming light toned to white mineral fills, one forming dark toned to grey mineral fills and one forming thin fins of protruding material (Kronyak *et al*., 2015). Here we apply PRo3D to mapping and structural analysis of vein systems exposed at Garden City (Kronyak *et al*., 2015; Young & Chan, 2017; Schwenzer *et al*., 2016; Nachon *et al*., 2017), visited by MSL on Sols 923 and 926, shortly after the Pahrump Hills campaign (Grotzinger *et al*., 2015, location in Fig. 2c). PRo3D enables quantitative analysis of a 3D outcrop model of the vein networks. The fractures and veins can be mapped out, lengths and widths (apertures) can be measured, together with the dip and strike of vein and fracture surfaces, and bedding surfaces.

Mastcam OPCs from Sol 923 and Mastcam and Navcam OPCs from Sol 926 were merged (Fig. 7a), allowing for understanding of the topographic context of the Garden City outcrop. The target Garden City is located in a valley called Artists' Drive. The floor and the slopes of this valley are formed from numerous outcrops of light-toned laminated mudstone with abundant fractures. The mudstone is overlain by a prominent weathering dark-toned, moderately well bedded sandstone, which forms small scarps at the top of the small cliffs in the area (Fig. 7a). The fractures are infilled by a mineral, which in some places causes it to weather proud from the surrounding mudstones. ChemCam analyses are consistent with this mineral being calcium sulphate (Kronyak *et al*., 2015; Nachon *et al*., 2014, 2017; Young & Chan 2017). The fractures and veins are highly interconnected, and tip to tip lengths cannot be measured. The lengths of individual segments were measured however, together with the dip and strike of veins and fractures with sufficient 3D topography, and the orientation of fracture traces at the surface. Detailed interpretations were digitised on the higher resolution Mastcam data in PRo3D, and some interpretation was carried out on the Navcam data, though in the latter case less detail could be achieved.

A 16 x 10 m area was interpreted from Navcam data, with a 2 x 1.5 m area in the centre covered by Mastcam data. The veins in the Mastcam data were exposed in an east-west trending outcrop. The mapped vein and fracture systems are shown in Figure 7b. Vein boundaries were digitised using a red polyline, and non-filled fractures were digitised with black polylines. Gaps in the interpretation are due to poor exposure, preservation, or data quality. Individual fracture segments are up to 2.5 m long. The mineralised vein assemblages show up to 9 cm of relief around the surrounding mudstones.

An equal distance rose diagram of the measured fracture trace azimuths is shown in Figure 7b. Maxima were identified at 170º-350º, 030º-210º, 080º-260º, and 120º-300º. The most prominent of these maxima were at 170º-350º and 080º-260º. The spread is consistent

with a polygonal fracture system, consisting of two orthogonal fracture sets, and two oblique ones. The results are comparable to fracture trace directions presented in Young and Chan (2017), but PRo3D has allowed a larger population of data to be collected, and therefore shows a larger variability in trace orientations. Measured fracture (white circles) and bedding dips (black circles) were plotted in a stereonet (Fig. 7c) showing clusters striking 098º and dipping 65º north, as well as striking 241º and dipping 71º to the south.

Aperture, the perpendicular distance between fracture walls, was calculated at intervals along an individual vein at which both boundaries could be clearly identified. 523 measurements were collected, and corrected for their slope by applying a cosine function to obtain the horizontal distance. Values ranged from 1.6 mm to 9.6 cm. The widest apertures were found in veins striking 050º-140º, and 080º-260º. Length vs aperture relationships are very important fracture analyses, and can provide information on the fluid pressures required to open the fractures, and the mechanical properties of the surrounding rocks. However, in this case the lack of veins preserved for their full trace length precludes this. Useful fracture outcrop length measurements require that the fracture must be continuous with both ends exposed and unrestricted by other discontinuities (Gudmundsson 2001). The highly connected fracture networks at Garden City preclude such an analysis.

These PRo3D analyses provide context for the mineralogical investigations which have taken place on the Garden City vein systems. Understanding of the orientations (fracture trace azimuths as well as dip and strike), and magnitudes (aperture) of the stresses involved in vein formation aids understanding of the relevance of these fracture systems to the evolution of Mars; whether they were formed as a result of tectonic stresses, fluid processes or exhumation.

6. Comparison and validation of PRo3D with prior research at Victoria crater, Meridiani Planum

The MER-B *Opportunity* Rover (2004-to time of writing) also carries a Pancam stereo panoramic camera system, and work has been carried out by previous authors on geological analysis of stereo-reconstructions of MER data. This provides an opportunity to test the results we have obtained carrying out similar analyses in PRo3D, with the results from previous work.

Victoria crater (Fig. 2d) is a ~ 750 m wide, moderately degraded, simple crater (Grant *et al*., 2008) located at 2.05°S, 5.50°W in the equatorial Meridiani Planum region of Mars. It

was visited by the *Opportunity* Rover, between Sols 952 and 1634 of operation. Approximately 100 – 150 m of erosional widening (Grant *et al*., 2008) has produced <15 m tall outcrops of pre-impact aeolian sedimentary rocks of the Burns formation, which form the upper dry section of a dry-wet-dry depositional sequence (Grotzinger *et* al., 2005; Hayes *et al*., 2011). Three members of the upper part of the ~20 m thick Burns formation have been identified in the sedimentary succession exposed at Victoria crater (Edgar *et al*., 2012); the Lyell, Smith and Steno members. Full 3D outcrops exposed in the promontories of the crater wall show 3 – 7 m thick bedsets of large-scale cross-bedding previously interpreted and analysed by Hayes *et al*., (2011). These outcrops provide an excellent opportunity to assess the capabilities of PRo3D in a comparative analysis.

A reference section was imaged at Duck Bay at close range by the Pancam system, but the rock outcrops within the scalloped bays and capes around Victoria crater were typically imaged from 50 – 70 m distance, precluding the use of fixed-baseline stereo processing due to heavy degradation of the fixed (30 cm) baseline stereo results at such large distance. Therefore, outcrops which were imaged more than once from different stations were chosen for wide-baseline stereo processing and subsequent analysis in PRo3D.

Previous three-dimensional analysis of stratal geometries at Victoria crater used MATlab® codes to co-register stereo Pancam images and a Principal Component Analysis (PCA) approach to dip and strike calculation (Edgar et al., 2012; Hayes et al., 2011). This enabled quantitative measurement of the dimensions and geometries of the sedimentary features at the outcrops there. Here we compare measurements determined using PRo3D, with prior measurements presented in Edgar *et al*., (2012) and Hayes *et al*., (2011).

6.1. Duck Bay

The PRo3D interpretation of Duck Bay made in this research is shown in Figure 8a, and the results are summarized in Supplementary Information Table S2a, alongside the results from Edgar *et al*., (2012). Three stratigraphic units were identified and correlated with those described by Edgar *et* al., (2012); the >0.9 m thick Lyell member at the base, which was characterised by a rough texture, pinstripe cross-laminations and a relatively dark colour (Fig. 8ai); the 0.5 m thick Smith member, which showed a gradational lower boundary, a lack of visible laminations and a smoother texture than the Lyell; and the 0.6 m thick Steno member at the top which is characterised by a lighter colour than the Lyell, but darker than the Smith and well preserved trough cross-laminations (Fig. 8aii). The topographic slope was calculated by reading the slope value of lines digitised on the floor of Duck Bay, within each

identified stratigraphic unit (Fig. 8a). Values range between 12º and 25º in the Lyell and Smith members, and up to 29º in the Steno member, which has a more prominent topographic expression, suggesting that the Steno member is more resistant to weathering, potentially as it is better cemented than the Smith member.

The upper boundary of the Lyell member was calculated in PRo3D to dip at 2º to the SW (~246º) based on two measurements (TL in "Boundaries" stereonet, inset in Fig. 8a). These results differ from those presented in Edgar *et al*., (2012), who also measured a dip of 2º, to the west, though the exact dip direction was not presented. Dips calculated in PRo3D on the Smith-Steno contact (BS in the "Boundaries" stereonet inset in Fig. 8a) were ~24º to the ESE (~110º), which was higher than the 10º to the SSE presented in Edgar *et al*., (2012). This is likely the expression of gentle undulations along the boundary, as the Smith member can be traced around the crater in HiRISE images (Fig. 2d), as well as other DOMs around the crater (such as Cape Desire, Fig. 8b).

Dip and strike measurements were also taken on the cross-laminations observed in the Lyell and Steno members at Duck Bay ("Internal laminations" in Fig. 8a) for comparison with those in Edgar *et al*., (2012). The rose diagram of orientation data from this research taken in PRo3D are shown inset in Figure 8a, and indicate bimodal dip azimuths with one dip azimuth to the ESE and a minor one to the WSW. This suggests a predominant palaeotransport direction of dunes to the ESE, with a a minor flow component to the WSW. This result is broadly comparable with the dip values presented in Edgar *et al*., (2012).

6.2. Cape Desire

Hayes *et al*., (2011) studied the sedimentary geometries of Cape Desire in detail (Fig. 8b). Here, a quantitative comparison is made between the results obtained through outcrop analysis in PRo3D (Fig. 8a) and those made by Hayes *et al*., (2011) (summarised with these results in Supplementary Information Table S2b). A 13 m thick vertical section was exposed, and the lateral extent at the top of the outcrop was 30 m, down to 10 m at the base where the outcrop is obscured by tallus. Hayes *et al*., (2011) identified 3 units through observation of truncation of laminations against the upper boundary (Units I – III in their paper). This study identified the stratigraphy mapped at Duck Bay by Edgar *et al*., (2012). The Lyell Member is up to 12.8 m thick vertically, and is characterised by abundant cross-laminations. The 0.4 – 0.7 m thick Smith Member is identified by its light colour and weathering profile, which is more apparent than in the 2D images. The Steno Member is fractured and thinly laminated, and varies in thickness from 0.8 – 1.1 m.

The Lyell Member (Fig. 8b) consists of five bedsets, which range between $1.7 - 3.7$ m thickness. They were identified using lamination truncations and observations of the weathering profile in 3D. Hayes *et al.*, (2011) determined the combined thickness of the Smith and Steno members to be between 1.4 to 1.6 m thick. In this study, the top Lyell boundary dips 6º towards 285º, the top Smith boundary dips 4º towards 263º, and the top Steno boundary dips 5º towards 264º (W). These values are summarised in Supplementary Information Table S2, and shown in the inset in Figure 8b ("Boundaries" stereonet). Plotting these values as poles to planes in a stereonet (Fig. 8b) shows that they are approximately conformable, unlike the Smith-Steno boundary (Fig. 8b), consistent with the interpretation that this is a gently undulating erosion surface.

Three dominant directions were observed in the cross-laminations within the Lyell unit ('All cross-laminations' rose diagram, inset to Fig. 8b), trending towards 270^0, 320^0-360^0 and 216^0, with lesser peaks observed towards 010^0, 080^0 and 140^0. This is comparable to observations by Hayes *et al.*, (2011). The palaeotransport directions in bedsets I – IV (Fig. 8b) vary up section. Unit IV shows a dominantly N-NW palaeotransport direction, trending between 310^0 and 360^0. Unit III show dominant trends towards 270^0 and 220. This swings to 340^0 and 010^0 in Unit II with Unit I showing peaks at 140^0 and 090^0. The results presented here are quite different to those in Hayes *et al.*, (2011), possibly as a result of dip and strike collection on different surfaces, providing different overall results.

6.3. Discussion and summary of results from Victoria crater

The difference in dip value of the base of the Steno member between Duck Bay and Cape Desire indicates that the boundary is undulating, but is continuous around the crater, because the light-toned Smith member is visible at Cape Desire and in HiRISE images at other locations around the crater. This evidence is consistent with the interpretation of an erosion surface at the base of Steno member as suggested by Edgar *et al.*, (2012). The thickness of the bedsets in the Lyell member at Cape Desire, combined with the cross-laminations at Duck Bay (Fig. 8ai), fine grain size, and good sorting (visible in Microscopic Imager data, not shown here – Edgar *et al.*, 2012) are consistent with the aeolian paleoenvironment interpretation of Edgar *et al.* (2012). It is inferred that the Smith member was deposited in the same environment as the Lyell, but was subject to a diagenetic episode which affected a $0.4 - 0.7$ m thick preserved section prior to deposition of the Steno member. Sufficient data was not present to determine the depositional environment of the Steno

member at both Duck Bay and Cape Desire (see Edgar *et al*., (2012) for a detailed description of the Steno member sedimentology). The variations in dominant transport directions shown in the rose diagram in Figure 8b in units I-IV of the Lyell Member at Cape Desire could be the result of changing wind directions through time, or a result of the deposition of sinuous crested sand dunes, forming trough cross stratified sets with variable dip directions.

The findings in this research show broadly comparable results to those previously published from Duck Bay and Cape Desire, particularly in that the dip value increases down section at Cape Desire to values that are above the angle of repose for those sediments. However, the values of up to 60° calculated in Hayes *et al*., (2011) are not replicated here, and values taken from the same location in PRo3D do not exceed 33°, in the same dip direction. This is consistent with the maximum angle of repose of modern aeolian sand dunes on the MSL traverse reported in Ewing *et al.,* (2017), where grainfall is present. Therefore, this does not fit with existing interpretations that the dip is above the angle of repose so must have been deformed. Outcrop geometries do not fit with this observation, and here we interpret that it is more likely that these dips represent the lee slopes of an ancient dune. It should be pointed out that low topographic relief on the surfaces makes it likely that the measured values may have some considerable error.

PRo3D shows results which are geometrically consistent within the viewer (relative to the up and north reference vectors), and comparable to previous results. Quality control using the plane visualisation on the dip and strike tool allows for a qualitative selection of the best locations for data collection. Future versions of PRo3D will incorporate expected uncertainty in OPC construction and location, as well as real-time dip and strike quality of fit and uniqess of fit visualisation. For this paper, we have quantified the OPC resolution, location uncertainty and the uncertainty associated with plane fitting for dip and strike measurement separately, and the data is presented in the Supplementary Information.

7. Summary

In summary, we show that the PRo3D visualisation tool enables repeatable quantitative analysis of planetary rover-derived stereo imagery datasets than is possible through analysis of 2D panoramas traditionally used to interpret the surface geology from rover and lander missions. The ability to place spatially-referenced image datasets from several different locations and then to roam the outcrop in 3D allows the user a first pass understanding of the 3D geometric relationships of the outcrop, and the spatial relationships of important geological features. The ability to measure 3D structural information from the

OPC surfaces assists in analysis and interpretation of the depositional geometries, and in elucidating characteristics such as palaeotransport direction. Additionally, line measurements of features such as bed thickness and grain size permit the application of detailed statistical analysis. All these factors lead to the potential for more quantitative analyses of the sedimentary geology of the rocks encountered during planetary rover missions. The absolute uncertainty of these measurements is currently unknown directly, as obviously it is not possible to groundtruth such data on Mars by humans yet. Further work for validation of PRo3D and the OPC data is ongoing for application to data derived from panoramic camera systems on future Mars rovers, such as the ExoMars 2020 rover.

References

Adams E. W., Bellian J. A., Milroy P., Reyes R. (2009) Supervised automated LiDAR mapping of Permo-triassic strata, Jebel Akhdar, Paper presented at the American Association of Petroleum Geologists Annual Convention. Denver, Oman, 7–10 June

Alexander, D.A., Deen, R.G., Andres, P.M., Zamani, P., Mortensen, H.B., Chen, A.C., Cayanan, M.K., Hall, J.R., Klochko, V.S., Pariser, O., Stanley, C.L., Thompson, C.K., Yagi, G.M., (2006). Processing of Mars Exploration Rover imagery for science and operations planning. J. Geophys. Res. 111, E02S02. doi:10.1029/2005JE002462

Allmendinger, R. W., Cardozo, N. C., and Fisher, D., (2013), Structural Geology Algorithms: Vectors & Tensors: Cambridge, England, Cambridge University Press, 289 pp

Almeida, R. P., Freitas, B. T., Turra, B. B., Figueiredo, F. T., Marconato, A. and Janikian, L. (2016), Reconstructing fluvial bar surfaces from compound cross-strata and the interpretation of bar accretion direction in large river deposits. Sedimentology, 63: 609–628. doi:10.1111/sed.12230

Anderson, R., Bridges, J. C., Williams, a., Edgar, L., Ollila, a., Williams, J., Vaniman, D. and the MSL Science Team (2015). ChemCam results from the Shaler outcrop in Gale crater, Mars. Icarus, 249, 2–21. doi:10.1016/j.icarus.2014.07.025

Arvidson, R.E., Anderson, R.C., Haldemann, A.F.C., Landis, G.A., Li, R., Lindemann, R.A., Matijevic, J.R., Morris, R.V., Richter, L., Squyres, S.W., Sullivan, R.J., Snider, N.O., 2003. Physical properties and localization investigations associated with the 2003 Mars Exploration rovers. J.-Geophys.-Res. 108, 8070. doi:10.1029/2002JE002041

Arvidson, R.E., Ashley, J.W., Bell, J.F., Chojnacki, M., Cohen, J., Economou, T.E., Farrand, W.H., Fergason, R., Fleischer, I., Geissler, P., Gellert, R., Golombek, M.P., Grotzinger, J.P., Guinness, E.A., Haberle, R.M., Herkenhoff, K.E., Herman, J.A., Iagnemma, K.D., Jolliff, B.L., Johnson, J.R., Klingelhöfer, G., Knoll, A.H., Knudson, A.T., Li, R., McLennan, S.M., Mittlefehldt, D.W., Morris, R.V., Parker, T.J., Rice, M.S., Schröder, C., Soderblom, L.A., Squyres, S.W., Sullivan, R.J., Wolff, M.J., 2011. *Opportunity* Mars Rover mission: Overview and selected results from Purgatory ripple to traverses to Endeavour crater. J. Geophys. Res. 116, E00F15. doi:10.1029/2010JE003746

Arvidson, R.E., Squyres, S.W., Bell, J.F., Catalano, J.G., Clark, B.C., Crumpler, L.S., Souza, P.A. de, Fairén, A.G., Farrand, W.H., Fox, V.K., Gellert, R., Ghosh, A., Golombek, M.P., Grotzinger, J.P., Guinness, E.A., Herkenhoff, K.E., Jolliff, B.L., Knoll, A.H., Li, R., McLennan, S.M., Ming, D.W., Mittlefehldt, D.W., Moore, J.M., Morris, R.V., Murchie, S.L., Parker, T.J., Paulsen, G., Rice, J.W., Ruff, S.W., Smith, M.D., Wolff, M.J., 2014. Ancient Aqueous Environments at Endeavour Crater, Mars. Science 343, 1248097. doi:10.1126/science.1248097

Arvidson, R.E., 2016. Aqueous history of Mars as inferred from landed mission measurements of rocks, soils, and water ice. J. Geophys. Res. Planets 121, 2016JE005079. doi:10.1002/2016JE005079

Banham, S. G., Gupta, S. , Rubin, D. M., Watkins, J. A., Sumner, D. Y., Edgett, K. S., Grotzinger, J. P., Lewis, K. W., Edgar, L. A., Stack-Morgan, K. M., Barnes, R. , Bell, J. F., Day, M. D., Ewing, R. C., Lapotre, M. G., Stein, N. T., Rivera-Hernandez, F. and Vasavada, A. R. (2018), Ancient Martian aeolian processes and palaeomorphology reconstructed from the Stimson formation on the lower slope of Aeolis Mons, Gale crater, Mars. Sedimentology. . doi:10.1111/sed.12469.Bell, J. F., Joseph, J., Sohl-Dickstein, J. N., Arneson, H. M., Johnson, M. J., Lemmon, M. T., & Savransky, D. (2006). In-flight calibration and performance of the Mars Exploration Rover Panoramic Camera (Pancam) instruments. Journal of Geophysical Research E: Planets, 111(2), 1–38. doi:10.1029/2005JE002444

Bell, J.F., Godber, A., McNair, S., Caplinger, M.A., Maki, J.N., Lemmon, M.T., Van Beek, J., Malin, M.C., Wellington, D., Kinch, K.M., Madsen, M.B., Hardgrove, C., Ravine, M.A., Jensen, E., Harker, D., Anderson, R.B., Herkenhoff, K.E., Morris, R.V., Cisneros, E., Deen, R.G., n.d. The Mars Science Laboratory *Curiosity* Rover Mast Camera (Mastcam) Instruments: Pre-Flight and In-Flight Calibration, Validation, and Data Archiving. Earth and Space Science 2016EA000219. doi:10.1002/2016EA000219

Bellian J. A., Kerans C., Jennette D. C. (2005) Digital Outcrop Models: applications of terrestrial scanning lidar technology in stratigraphic modeling. Journal of Sedimentary Research 72:166–176.

Blaney, D.L., Wiens, R.C., Maurice, S., Clegg, S.M., Anderson, R.B., Kah, L.C., Le Mouélic, S., Ollila, A., Bridges, N., Tokar, R., Berger, G., Bridges, J.C., Cousin, A., Clark, B., Dyar, M.D., King, P.L., Lanza, N., Mangold, N., Meslin, P.-Y., Newsom, H., Schröder, S., Rowland, S., Johnson, J., Edgar, L., Gasnault, O., Forni, O., Schmidt, M., Goetz, W., Stack, K., Sumner, D., Fisk, M., Madsen, M.B., 2014. Chemistry and texture of the rocks at Rocknest, Gale Crater: Evidence for sedimentary origin and diagenetic alteration. J. Geophys. Res. Planets 119, 2013JE004590. doi:10.1002/2013JE004590

Bristow T.F., Bish D.L., Vaniman D.T., Morris R.V., Blake D.F., Grotzinger J.P., Rampe E.B., Crisp J.A., Achilles C.N., Ming D.W., Ehlmann B.L., King P.L., Bridges J.C., Eigenbrode J.L., Sumner D.Y., Chipera S.J., Moorokian J.M., Treiman A.H., Morrison S.M., Downs R.T., Farmer J.D., Des M.D., Sarrazin P., Floyd M.M., Mischna M.A., McAdam A.C., (2015), The origin and implications of clay minerals from Yellowknife Bay, Gale crater, Mars. American Mineralogist 100, 824–836. doi:10.2138/am-2015-5077CCBYNCND

Buckley, S.J. Howell, J.A. Enge, H. D. Leren, B. L. S. and Kurz, T. H. (2006) Integration of terrestrial laser scanning, digital photogrammetry and geostatistical methods forhigh-resolution modelling of geological outcrops. International Archives of the Photogrammetry, Remote Sensing and Spatial Information Science, 36(B5),.

Buckley, S. J., Howell, J. A., Enge, H. D., and Kurz, T. H.: Terrestrial laser scanning in geology: data acquisition, processing and accuracy considerations, (2008a). J. Geol. Soc., 165, 625–638,https://doi.org/10.1144/0016-76492007-100,

Buckley S., Vallet J., Braathen A., Wheeler W. (2008b) Oblique helicopter-based laser scanning for digital terrain modelling and visualisation of geological outcrops. International Archives of the Photogrammetry, Remote Sensing and Spatial Information Sciences XXXVII:493–498.

Burton D., Wood L. (2011) Quantitative characterization of the tidally influenced Sego Sandstone. American Association of Petroleum Geologists Bulletin 95:1207–1226.

Cardozo, N., and Allmendinger, R. W., 2013, Spherical projections with OSXStereonet: Computers & Geosciences, v. 51, no. 0, p. 193 - 205, doi: 10.1016/j.cageo.2012.07.021

Clark, B.C., Morris, R.V., Herkenhoff, K.E., Farrand, W.H., Gellert, R., Jolliff, B.L., Arvidson, R.E., Squyres, S.W., Mittlefehldt, D.W., Ming, D.W., Yen, A.S., 2016. Esperance: Multiple episodes of aqueous alteration involving fracture fills and coatings at Matijevic Hill, Mars. American Mineralogist 101, 1515–1526. doi:10.2138/am-2016-5575

Collinson, J.D., Mountney, N., Thompson, D.B., 2006. Sedimentary Structures. Terra Pub.

Crumpler, L.S., Arvidson, R.E., Squyres, S.W., McCoy, T., Yingst, A., Ruff, S., Farrand, W., McSween, Y., Powell, M., Ming, D.W., Morris, R.V., Bell, J.F., Grant, J., Greeley, R., DesMarais, D., Schmidt, M., Cabrol, N.A., Haldemann, A., Lewis, K.W., Wang, A.E., Schröder, C., Blaney, D., Cohen, B., Yen, A., Farmer, J., Gellert, R., Guinness, E.A., Herkenhoff, K.E., Johnson, J.R., Klingelhöfer, G., McEwen, A., Rice, J.W., Rice, M., deSouza, P., Hurowitz, J., 2011. Field reconnaissance geologic mapping of the Columbia Hills, Mars, based on Mars Exploration Rover Spirit and MRO HiRISE observations. J. Geophys. Res. 116, E00F24. doi:10.1029/2010JE003749

Crumpler, L.S., Arvidson, R.E., Bell, J., Clark, B.C., Cohen, B.A., Farrand, W.H., Gellert, R., Golombek, M., Grant, J.A., Guinness, E., Herkenhoff, K.E., Johnson, J.R., Jolliff, B., Ming, D.W., Mittlefehldt, D.W., Parker, T., Rice, J.W., Squyres, S.W., Sullivan, R., Yen, A.S., 2015. Context of ancient aqueous environments on Mars from in situ geologic mapping at Endeavour Crater. J. Geophys. Res. Planets 120, 2014JE004699. doi:10.1002/2014JE004699

Davison, I., 1995. Fault slip evolution determined from crack-seal veins in pull-aparts and their implications for general slip models. Journal of Structural Geology 17, 1025–1034. doi:10.1016/0191-8141(94)00131-I

DeCelles, P.G., Langford, R.P., Schwartz, R.K., 1983. Two New Methods of Paleocurrent Determination from Trough Cross-Stratification. Journal of Sedimentary Research 53.

Dott, R.H. (1973) Paleocurrent analysis of trough cross stratification. Journal of Sedimentary Petrology, 43, 779-783.

Edgar, L. A., Grotzinger, J. P., Hayes, A. G., Rubin, D. M., Squyres, S. W., Bell, J. F., and K. E. Herkenhoff, Stratigraphic Architecture of Bedrock Reference Section, Victoria Crater, Meridiani Planum, Mars, SEPM Special Publication 102, Sedimentary Geology of Mars, 195-209. 2012

Edgar, L.A., Grotzinger, J.P., Bell, J.F., Hurowitz, J.A., 2014. Hypotheses for the origin of fine-grained sedimentary rocks at Santa Maria crater, Meridiani Planum. Icarus 234, 36–44. doi:10.1016/j.icarus.2014.02.019

Edgar, L. A., Gupta, S., Rubin, D. M., Lewis, K. W., Kocurek, G. A., Anderson, R. B., Bell, J. F., Dromart, G., Edgett, K. S., Grotzinger, J. P., Hardgrove, C., Kah, L. C., Leveille, R., Malin, M. C., Mangold, N., Milliken, R. E., Minitti, M., Palucis, M., Rice, M., Rowland, S. K., Schieber, J., Stack, K. M., Sumner, D. Y., Wiens, R. C., Williams, R. M. E. and Williams, A. J. (2017), Shaler: *in situ* analysis of a fluvial sedimentary deposit on Mars. Sedimentology. doi:10.1111/sed.12370

Enge H. D., Buckley S. J., Rotevatn A., Howell J. A. (2007) From outcrop to reservoir simulation model: workflow and procedures. Geosphere 3:469–490.

Fabuel-Perez I., Hodgetts D., Redfern J. (2009a) A new approach for outcrop characterization and geostatistical analysis of a low-sinuosity fluvial-dominated succession using Digital Outcrop Models: Upper Triassic Oukaimeden Sandstone Formation, Central High Atlas, Morocco. American Association of Petroleum Geologists Bulletin 93:795–827.

Fox, J.M. and McCurdy, M. (2007) Activity planning for the Phoenix Mars lander mission, in *Aerospace Conference, 2007 IEEE*, IEEE, pp. 1–13.

Glotch, T.D., Bandfield, J.L., Christensen, P.R., Calvin, W.M., McLennan, S.M., Clark, B.C., Rogers, A.D., Squyres, S.W., 2006. Mineralogy of the light-toned outcrop at Meridiani Planum as seen by the Miniature Thermal Emission Spectrometer and implications for its formation. J. Geophys. Res. 111, E12S03. doi:10.1029/2005JE002672

Grant, J.A., Wilson, S.A., Cohen, B.A., Golombek, M.P., Geissler, P.E., Sullivan, R.J., Kirk, R.L., Parker, T.J., 2008. Degradation of Victoria crater, Mars. Journal of Geophysical Research E: Planets 113, E11010. doi:10.1029/2008JE003155

Grotzinger, J.P., Arvidson, R.E., Bell III, J.F., Calvin, W., Clark, B.C., Fike, D.A., Golombek, M., Greeley, R., Haldemann, A., Herkenhoff, K.E., Jolliff, B.L., Knoll, A.H., Malin, M., McLennan, S.M., Parker, T., Soderblom, L., Sohl-Dickstein, J.N., Squyres, S.W., Tosca, N.J., Watters, W.A., 2005. Stratigraphy and sedimentology of a dry to wet eolian depositional system, Burns formation, Meridiani Planum, Mars. Earth and Planetary Science Letters, Sedimentary Geology at Meridiani Planum, Mars 240, 11–72. doi:10.1016/j.epsl.2005.09.039

Grotzinger, J., Bell, J., Herkenhoff, K., Johnson, J., Knoll, A., McCartney, E., McLennan, S., Metz, J., Moore, J., Squyres, S., Sullivan, R., Ahronson, O., Arvidson, R., Joliff, B., Golombek, M., Lewis, K., Parker, T., Soderblom, J., 2006. Sedimentary textures formed by aqueous processes, Erebus crater, Meridiani Planum, Mars. Geology 34, 1085–1088. doi:10.1130/G22985A.1

Grotzinger, J.P., Crisp, J., Vasavada, A.R., Anderson, R.C., Baker, C.J., Barry, R., Blake, D.F., Conrad, P., Edgett, K.S., Ferdowski, B., Gellert, R., Gilbert, J.B., Golombek, M., Gómez-Elvira, J., Hassler, D.M., Jandura, L., Litvak, M., Mahaffy, P., Maki, J., Meyer, M., Malin, M.C., Mitrofanov, I., Simmonds, J.J., Vaniman, D., Welch, R.V., Wiens, R.C., 2012. Mars Science Laboratory Mission and Science Investigation. Space Sci Rev 170, 5–56. doi:10.1007/s11214-012-9892-2

Grotzinger, J. P., Sumner, D. Y., Kah, L. C., Stack, K., Gupta, S., Farmer, J. and the MSL Science Team (2014). A Habitable Fluvio-Lacustrine Environment at Yellowknife Bay, Gale Crater, Mars, , Science, 343 (6169), 1–15.

Grotzinger, J.P., Gupta, S., Malin, M.C., Rubin, D.M., Schieber, J., Siebach, K., Sumner, D.Y., Stack, K.M., Vasavada, A.R., Arvidson, R.E., Calef, F., Edgar, L., Fischer, W.F., Grant, J.A., Griffes, J., Kah, L.C., Lamb, M.P., Lewis, K.W., Mangold, N., Minitti, M.E., Palucis, M., Rice, M., Williams, R.M.E., Yingst, R.A., Blake, D., Blaney, D., Conrad, P., Crisp, J., Dietrich, W.E., Dromart, G., Edgett, K.S., Ewing, R.C., Gellert, R., Hurowitz, J.A., Kocurek, G., Mahaffy, P., McBride, M.J., McLennan, S.M., Mischna, M., Ming, D., Milliken, R., Newsom, H., Oehler, D., Parker, T.J., Vaniman, D., Wiens, R.C., Wilson, S.A., 2015. Deposition, exhumation, and paleoclimate of an ancient lake deposit, Gale crater, Mars. Science 350, aac7575. doi:10.1126/science.aac7575

Gudmundsson, A., 2001. Fluid overpressure and flow in fault zones: field measurements and models. Tectonophysics 336, 183–197. doi:10.1016/S0040-1951(01)00101-9

Hartzell, P., Glennie, C., Biber, K., Khan, S., 2014. Application of multispectral LiDAR to automated virtual outcrop geology. ISPRS Journal of Photogrammetry and Remote Sensing 88, 147–155. doi:10.1016/j.isprsjprs.2013.12.004

Hayes, a. G., Grotzinger, J. P., Edgar, L. a., Squyres, S. W., Watters, W. a., & Sohl-Dickstein, J. (2011). Reconstruction of eolian bed forms and paleocurrents from

cross-bedded strata at Victoria Crater, Meridiani Planum, Mars. Journal of Geophysical Research E: Planets, 116(4), 1–17. doi:10.1029/2010JE003688

High, L.R. and Picard, M.D. (1974) Reliability of cross-stratification types as paleocurrent indicators in fluvial rocks. Journal of Sedimentary Petrology, 44, 158-168.

Hodgetts, D., 2013. Laser scanning and digital outcrop geology in the petroleum industry: A review. Marine and Petroleum Geology 46, 335–354. doi:10.1016/j.marpetgeo.2013.02.014

Hurowitz, J.A., Fischer, W.W., Tosca, N.J., Milliken, R.E., 2010. Origin of acidic surface waters and the evolution of atmospheric chemistry on early Mars. Nature Geoscience, 323–326. doi:10.1038/ngeo831

Kah, L.C., Kronyak, R., Van Beek, J., Nachon, M., Mangold, N., Thompson, L., Wiens, R., Grotzinger, J., Farmer, J., Minitti, M., Shieber, J., Oehler, D., 2015. Diagenetic Crystal Clusters and Dendrites, Lower Mount Sharp, Gale Crater. Presented at the Lunar and Planetary Science Conference, 16-20 Mar. 2015, United States.

Knauth, L.P., Burt, D.M., Wohletz, K.H., 2005. Impact origin of sediments at the *Opportunity* landing site on Mars. Nature 438, 1123–1128. doi:10.1038/nature04383

Kneissl, T., van Gasselt, S., Neukum, G., 2010. Measurement of Strike and Dip of Geologic Layers from Remote Sensing Data — New Software Tool for ArcGIS. Presented at the Lunar and Planetary Science Conference, p. 1640.

Knoll, A.H., Jolliff, B.L., Farrand, W.H., Bell, J.F., Clark, B.C., Gellert, R., Golombek, M.P., Grotzinger, J.P., Herkenhoff, K.E., Johnson, J.R., McLennan, S.M., Morris, R., Squyres, S.W., Sullivan, R., Tosca, N.J., Yen, A., Learner, Z., 2008. Veneers, rinds, and fracture fills: Relatively late alteration of sedimentary rocks at Meridiani Planum, Mars. J. Geophys. Res. 113, E06S16. doi:10.1029/2007JE002949

Kronyak, R.E., Kah, L.C., Grotzinger, J.P., Fisk, M.R., Sumner, D.Y., Nachon, M., Mangold, N., Blaney, D.L., Rapin, W. and Wiens, R.C. 2015. Garden City: a complex vein system observed by the *Curiosity* rover at Pahrump Hills, Gale crater, Mars. Paper presented at 2015 GSA Annual Meeting in Baltimore, Maryland, USA (1-4 November 2015).

Léveillé, R.J., Bridges, J., Wiens, R.C., Mangold, N., Cousin, A., Lanza, N., Forni, O., Ollila, A., Grotzinger, J., Clegg, S., Siebach, K., Berger, G., Clark, B., Fabre, C., Anderson, R., Gasnault, O., Blaney, D., Deflores, L., Leshin, L., Maurice, S., Newsom, H., (2014), Chemistry of fracture-filling raised ridges in Yellowknife Bay, Gale Crater: Window into past aqueous activity and habitability on Mars. J. Geophys. Res. Planets 119, 2014JE004620. doi:10.1002/2014JE004620

Lewis, K.W., Aharonson, O., Grotzinger, J.P., Squyres, S.W., Bell, J.F., Crumpler, L.S., Schmidt, M.E., 2008. Structure and stratigraphy of Home Plate from the Spirit Mars Exploration Rover. J. Geophys. Res. 113, E12S36. doi:10.1029/2007JE003025

Pringle, J.K., Brunt, R.L., Hodgson, D.M., Flint, S.S., 2010. Capturing stratigraphic and sedimentological complexity from submarine channel complex outcrops to digital 3D models, Karoo Basin, South Africa. Petroleum Geoscience 16, 307–330.

Maki, J.N., Bell, J.F., Herkenhoff, K.E., Squyres, S.W., Kiely, A., Klimesh, M., Schwochert, M., Litwin, T., Willson, R., Johnson, A., Maimone, M., Baumgartner, E., Collins, A., Wadsworth, M., Elliot, S.T., Dingizian, A., Brown, D., Hagerott, E.C., Scherr, L., Deen, R., Alexander, D., Lorre, J., 2003. Mars Exploration Rover Engineering Cameras. J.-Geophys.-Res. 108, 8071. doi:10.1029/2003JE002077

Maki, J., Thiessen, D., Pourangi, A., Kobzeff, P., Litwin, T., Scherr, L., Elliott, S., Dingizian, A. and Maimone, M. (2012) The Mars Science Laboratory Engineering Cameras. Space Science Reviews, 170, 77-93.

Malin, M.C., Ravine, M.A., Caplinger, M.A., Ghaemi, F.T., Schaffner, J.A., Maki, J.N., Bell, J.F., Cameron, J.F., Dietrich, W.E., Edgett, K.S., Edwards, L.J., Garvin, J.B., Hallet, B., Herkenhoff, K.E., Heydari, E., Kah, L.C., Lemmon, M.T., Minitti, M.E., Olson, T.S., Parker, T.J., Rowland, S.K., Schieber, J., Sletten, R., Sullivan, R.J., Sumner, D.Y., Yingst, R.A., Duston, B.M., McNair, S., Jensen, E.H., n.d. The Mars Science Laboratory (MSL) Mast Cameras and Descent Imager: I. Investigation and Instrument Descriptions. Earth and Space Science 2016EA000252. doi:10.1002/2016EA000252

Mangold, N., Forni, O., Dromart, G., Stack, K., Wiens, R.C., Gasnault, O., Sumner, D.Y., Nachon, M., Meslin, P.-Y., Anderson, R.B., Barraclough, B., Bell, J.F., Berger,

G., Blaney, D.L., Bridges, J.C., Calef, F., Clark, B., Clegg, S.M., Cousin, A., Edgar, L., Edgett, K., Ehlmann, B., Fabre, C., Fisk, M., Grotzinger, J., Gupta, S., Herkenhoff, K.E., Hurowitz, J., Johnson, J.R., Kah, L.C., Lanza, N., Lasue, J., Le Mouélic, S., Léveillé, R., Lewin, E., Malin, M., McLennan, S., Maurice, S., Melikechi, N., Mezzacappa, A., Milliken, R., Newsom, H., Ollila, A., Rowland, S.K., Sautter, V., Schmidt, M., Schröder, S., d'Uston, C., Vaniman, D., Williams, R., 2015. Chemical variations in Yellowknife Bay formation sedimentary rocks analyzed by ChemCam on board the *Curiosity* rover on Mars. J. Geophys. Res. Planets 120, 2014JE004681. doi:10.1002/2014JE004681

McCollom, T.M., Hynek, B.M., 2005. A volcanic environment for bedrock diagenesis at Meridiani Planum on Mars. Nature 438, 1129–1131. doi:10.1038/nature04390

McLennan, S.M., Bell III, J.F., Calvin, W.M., Christensen, P.R., Clark, B.C., de Souza, P.A., Farmer, J., Farrand, W.H., Fike, D.A., Gellert, R., Ghosh, A., Glotch, T.D., Grotzinger, J.P., Hahn, B., Herkenhoff, K.E., Hurowitz, J.A., Johnson, J.R., Johnson, S.S., Jolliff, B., Klingelhöfer, G., Knoll, A.H., Learner, Z., Malin, M.C., McSween Jr., H.Y., Pocock, J., Ruff, S.W., Soderblom, L.A., Squyres, S.W., Tosca, N.J., Watters, W.A., Wyatt, M.B., Yen, A., 2005. Provenance and diagenesis of the evaporite-bearing Burns formation, Meridiani Planum, Mars. Earth and Planetary Science Letters, Sedimentary Geology at Meridiani Planum, Mars 240, 95–121. doi:10.1016/j.epsl.2005.09.041

Metz, J. M., Grotzinger, J. P., Rubin, D. M., Lewis, K. W., Squyres, S. W., & Bell, J. F. (2009). Sulfate-Rich Eolian and Wet Interdune Deposits, Erebus Crater, Meridiani Planum, Mars. Journal of Sedimentary Research, 79(5), 247–264. doi:10.2110/jsr.2009.033

Michelson, P.C. and Dott, R.H. (1973) Orientation analysis of trough cross stratification in upper Cambrian sandstones of western Wisconsin. Journal of Sedimentary Petrology, 43, 784-794.

Minisini, D., Wang, M., Bergman, S.C., Aiken, C., 2014. Geological data extraction from lidar 3-D photorealistic models: A case study in an organic-rich mudstone, Eagle Ford Formation, Texas. Geosphere 10, 610–626. doi:10.1130/GES00937.1

Morris, R.V., Klingelhöfer, G., Schröder, C., Rodionov, D.S., Yen, A., Ming, D.W., de Souza, P.A., Fleischer, I., Wdowiak, T., Gellert, R., Bernhardt, B., Evlanov, E.N., Zubkov, B., Foh, J., Bonnes, U., Kankeleit, E., Gütlich, P., Renz, F., Squyres,

S.W., Arvidson, R.E., 2006. Mössbauer mineralogy of rock, soil, and dust at Gusev crater, Mars: Spirit's journey through weakly altered olivine basalt on the plains and pervasively altered basalt in the Columbia Hills. J. Geophys. Res. 111, E02S13. doi:10.1029/2005JE002584

Nachon, M., Clegg, S.M., Mangold, N., Schröder, S., Kah, L.C., Dromart, G., Ollila, A., Johnson, J.R., Oehler, D.Z., Bridges, J.C., Le Mouélic, S., Forni, O., Wiens, R. c., Anderson, R.B., Blaney, D.L., Bell, J. f., Clark, B., Cousin, A., Dyar, M.D., Ehlmann, B., Fabre, C., Gasnault, O., Grotzinger, J., Lasue, J., Lewin, E., Léveillé, R., McLennan, S., Maurice, S., Meslin, P.-Y., Rapin, W., Rice, M., Squyres, S.W., Stack, K., Sumner, D.Y., Vaniman, D., Wellington, D., 2014. Calcium sulfate veins characterized by ChemCam/*Curiosity* at Gale crater, Mars. J. Geophys. Res. Planets 119, 2013JE004588. doi:10.1002/2013JE004588

Nachon, M., Mangold, N., Forni, O., Kah, L.C., Cousin, A., Wiens, R.C., Anderson, R., Blaney, D., Blank, J.G., Calef, F., Clegg, S.M., Fabre, C., Fisk, M.R., Gasnault, O., Grotzinger, J.P., Kronyak, R., Lanza, N.L., Lasue, J., Deit, L.L., Mouélic, S.L., Maurice, S., Meslin, P.-Y., Oehler, D.Z., Payré, V., Rapin, W., Schröder, S., Stack, K., Sumner, D., 2017. Chemistry of diagenetic features analyzed by ChemCam at Pahrump Hills, Gale crater, Mars. Icarus 281, 121–136. doi:10.1016/j.icarus.2016.08.026

NASA (2015), Maestro, https://software.NASA.gov/featuredsoftware/maestro. Accessed: 2015-10-28.

NASA/JPL (2015), MSLICE, http://www.NASA.gov/centers/ames/research/MSL_operations_prt.htm. Accessed:2015-12-06.

Paar, G.; Waugh, L.; Barnes, D. P.; Pajdla, T.; Woods, M.; Graf, H.-R.; Gao, Y.; Willner, K.; Muller, J.-P. & Li, R. (2012), Integrated field testing of planetary robotics vision processing: the PRoVisG campaign in Tenerife 2011, *in* 'Proc. SPIE 8301, 83010O'.

Paar, G., et al. "PRoViDE: Planetary Robotics Vision Data Processing and Fusion." European Planetary Science Congress 2015, held 27 September-2 October, 2015 in Nantes, France, Online at http://meetingorganizer. copernicus. org/EPSC2015, id. EPSC2015-345. Vol. 10. 2015.

Pringle J. K., Howell J. A., Hodgetts D., Westermann A. R., Hodgson D. M. (2006) Virtual outcrop models of petroleum reservoir analogues: a review of the current state-of-the-art. First break 24:33–42.

Rarity, F., Lanen, X.M.T. van, Hodgetts, D., Gawthorpe, R.L., Wilson, P., Fabuel-Perez, I., Redfern, J., 2014. LiDAR-based digital outcrops for sedimentological analysis: workflows and techniques. Geological Society, London, Special Publications 387, 153–183. doi:10.1144/SP387.5

Rice, M.S., Gupta, S., Treiman, A.H., Stack, K.M., Calef, F., Edgar, L.A., Grotzinger, J., Lanza, N., Le Deit, L., Lasue, J., Siebach, K.L., Vasavada, A., Wiens, R.C., Williams, J., 2017. Geologic overview of the Mars Science Laboratory rover mission at the Kimberley, Gale crater, Mars. J. Geophys. Res. Planets 122, 2016JE005200. doi:10.1002/2016JE005200

Rubin, D.M., Hunter, R.E., 1983. Reconstructing Bedform Assemblages from Compound Crossbedding. Developments in Sedimentology, Eolian Sediments and Processes 38, 407–427. doi:10.1016/S0070-4571(08)70807-0

Ruff, S.W., Farmer, J.D., Calvin, W.M., Herkenhoff, K.E., Johnson, J.R., Morris, R.V., Rice, M.S., Arvidson, R.E., Bell, J.F., Christensen, P.R., Squyres, S.W., 2011a. Characteristics, distribution, origin, and significance of opaline silica observed by the Spirit rover in Gusev crater, Mars. J. Geophys. Res. 116, E00F23. doi:10.1029/2010JE003767

Reading, H.G., 2009. Sedimentary Environments: Processes, Facies and Stratigraphy. John Wiley & Sons.

Sahoo, H., Gani, N.D., 2015. Creating three-dimensional channel bodies in LiDAR-integrated outcrop characterization: A new approach for improved stratigraphic analysis. Geosphere 11, 777–785. doi:10.1130/GES01075.1

Siebach, K.L., Grotzinger, J.P., Kah, L.C., Stack, K.M., Malin, M., Léveillé, R., Sumner, D.Y., (2014), Subaqueous shrinkage cracks in the Sheepbed mudstone: Implications for early fluid diagenesis, Gale crater, Mars. J. Geophys. Res. Planets 119, 2014JE004623. doi:10.1002/2014JE004623.

Schieber, J., Bish, D., Coleman, M., Reed, M., Hausrath, E.M., Cosgrove, J., Gupta, S., Minitti, M.E., Edgett, K.S., Malin, M., 2017. Encounters with an unearthly

mudstone: Understanding the first mudstone found on Mars. Sedimentology 64, 311–358. doi:10.1111/sed.12318

Schwenzer, S.P., Bridges, J.C., Wiens, R.C., Conrad, P.G., Kelley, S.P., Leveille, R., Mangold, N., Martín-Torres, J., McAdam, A., Newsom, H., Zorzano, M.P., Rapin, W., Spray, J., Treiman, A.H., Westall, F., Fairén, A.G., Meslin, P.-Y., 2016. Fluids during diagenesis and sulfate vein formation in sediments at Gale crater, Mars. Meteorit Planet Sci 51, 2175–2202. doi:10.1111/maps.12668

Squyres, S. W., Arvidson, R. E., Bell, J. F., Brückner, J., Cabrol, N. a, Calvin, W., … Yen, a. (2004). The *Opportunity* Rover's Athena science investigation at Meridiani Planum, Mars. Science, 306(5702), 1698–1703. doi:10.1126/science.1106171

Squyres, S. W., Arvidson, R. E., Bell, J. F., Brückner, J., Cabrol, N. a, Calvin, W., … Yen, a. (2004). The Spirit Rover's Athena science investigation at Gusev Crater, Mars. Science, 305(5685), 794–799. doi:10.1126/science.3050794

Squyres, S. W., & Knoll, A. H. (2005). Sedimentary rocks at Meridiani Planum: Origin, diagenesis, and implications for life on Mars. Earth and Planetary Science Letters, 240 (1), 1–10. doi:10.1016/j.epsl.2005.09.038

Squyres, S.W., Arvidson, R.E., Ruff, S., Gellert, R., Morris, R.V., Ming, D.W., Crumpler, L., Farmer, J.D., Marais, D.J.D., Yen, A., McLennan, S.M., Calvin, W., Bell, J.F., Clark, B.C., Wang, A., McCoy, T.J., Schmidt, M.E., Souza, P.A. de, 2008. Detection of Silica-Rich Deposits on Mars. Science 320, 1063–1067. doi:10.1126/science.1155429

Stack, K.M., Grotzinger, J.P., Kah, L.C., Schmidt, M.E., Mangold, N., Edgett, K.S., Sumner, D.Y., Siebach, K.L., Nachon, M., Lee, R., Blaney, D.L., Deflores, L.P., Edgar, L.A., Fairén, A.G., Leshin, L.A., Maurice, S., Oehler, D.Z., Rice, M.S., and Wiens, R.C. (2014), Diagenetic origin of nodules in the Sheepbed member, Yellowknife Bay formation, Gale crater, Mars, J. Geophys. Res.: Planets, 119, 1637-1664, doi: 10.1002/2014JE004617.

Stack, K.M., Edwards, C.S., Grotzinger, J.P., Gupta, S., Sumner, D.Y., Calef III, F.J., Edgar, L.A., Edgett, K.S., Fraeman, A.A., Jacob, S.R., Le Deit, L., Lewis, K.W., Rice, M.S., Rubin, D., Williams, R.M.E., Williford, K.H., 2016. Comparing orbiter and rover image-based mapping of an ancient sedimentary environment, Aeolis Palus, Gale crater, Mars. Icarus, MicroMars to MegaMars 280, 3–21. doi:10.1016/j.icarus.2016.02.024

Tao, Y., and J.-P. Muller (2016a) A novel method for surface exploration: super-resolution restoration of Mars repeat-pass orbital imagery, Planetary and Space Science, Vol 121, p103-114, http://dx.doi.org/10.1016/j.pss.2015.11.010

Tao Y., Muller, J.-P. Poole W. (2016b) Automated localisation of Mars rovers using co-registered HiRISE-CTX-HRSC orthorectified images and wide baseline Navcam orthorectified mosaics, ICARUS, Vol 280, p139-157, http://dx.doi.org/10.1016/j.icarus.2016.06.017.

Van Bommel, S.J., Gellert, R., Berger, J.A., Campbell, J.L., Thompson, L.M., Edgett, K.S., McBride, M.J., Minitti, M.E., Pradler, I., Boyd, N.I., 2016. Deconvolution of distinct lithology chemistry through oversampling with the Mars Science Laboratory Alpha Particle X-Ray Spectrometer. X-Ray Spectrom. 45, 155–161. doi:10.1002/xrs.2681

van Lanen X. M. T., Hodgetts D., Redfern J., Fabuel-Perez I. (2009) Applications of Digital Outcrop Models: two fluvial case studies from the Triassic Wolfville Fm., Canada and Oukaimeden Sandstone Fm., Morocco. Geological Journal 44:742–760.

van Lanen X. M. T. (2010) Quantitative Outcrop Analysis and Modelling of The Triassic Fluvial Wolfville Formation (Nova Scotia, Canada) PhD thesis (University of Manchester, UK).

Vaniman, D.T., Bish, D.L., Ming, D.W., Bristow, T.F., Morris, R.V., Blake, D.F., Chipera, S.J., Morrison, S.M., Treiman, A.H., Rampe, E.B., Rice, M., Achilles, C.N., Grotzinger, J.P., McLennan, S.M., Williams, J., Bell, J.F., Newsom, H.E., Downs, R.T., Maurice, S., Sarrazin, P., Yen, A.S., Morookian, J.M., Farmer, J.D., Stack, K., Milliken, R.E., Ehlmann, B.L., Sumner, D.Y., Berger, G., Crisp, J.A., Hurowitz, J.A., Anderson, R., Marais, D.J.D., Stolper, E.M., Edgett, K.S., Gupta, S., Spanovich, N., Team, M.S. (2014), Mineralogy of a Mudstone at Yellowknife Bay, Gale Crater, Mars. Science 343, 1243480. doi:10.1126/science.1243480.

Vasavada, A. R. Grotzinger, J. P. Arvidson, R. E. Calef, F. J. Crisp, J. A. Gupta, S. Hurowitz, J. Mangold N., Maurice, S. Schmidt, M. E. Wiens, R. C. Williams R. M. E. and Yingst R. A. (2014) Overview of the Mars Science Laboratory Mission: Bradbury Landing to Yellowknife Bay and Beyond. J. Geophys. Res. Planets DOI: 10.1002/2014JE004622

Verwer K., Kenter J. A. M., Maathuis B., Della Porta G. (2004) in Geological Prior Information: Informing Science and Engineering, Stratal patterns and lithofacies of

an intact seismic-scale Carboniferous carbonate platform (Asturias, NW Spain): a virtual outcrop model, Geological Society, London, Special Publications, eds Curtis A. C., Wood R. M. 239, pp 29–41.

Viseur S., Richet R., Borgomano J., Adams E. W. (2007) Semi-automated detection of geological features from Digital Outcrop Models (the Gresse-en-Vercors Cliff, France) Paper presented at the 69th European Association of Geoscientists and Engineers Annual Conference and Exhibition, London, 11 June.

Vollmer, F. W., 1995. C program for automatic contouring of spherical orientation data using a modified Kamb method: Computers & Geosciences, v. 21, p. 31-49.

Vollmer, F.W., 2015. Orient 3: a new integrated software program for orientation data analysis, kinematic analysis, spherical projections, and Schmidt plots. Geological Society of America Abstracts with Programs, v. 47, n. 7, p. 49.

Watkins, J., Grotzinger J., Stein N., Banham S.G., Gupta, S. Rubin, D. Stack, K.M. Edgett K.S. (2016), Paleotopography of erosional unconformity, base of Stimson formation, Gale crater, Mars. 47th Lunar and Planetary Science Conference 2016.

Young, B.W., Chan, M.A., 2017. Gypsum veins in Triassic Moenkopi mudrocks of southern Utah: Analogs to calcium sulfate veins on Mars. J. Geophys. Res. Planets 122, 2016JE005118. doi:10.1002/2016JE005118
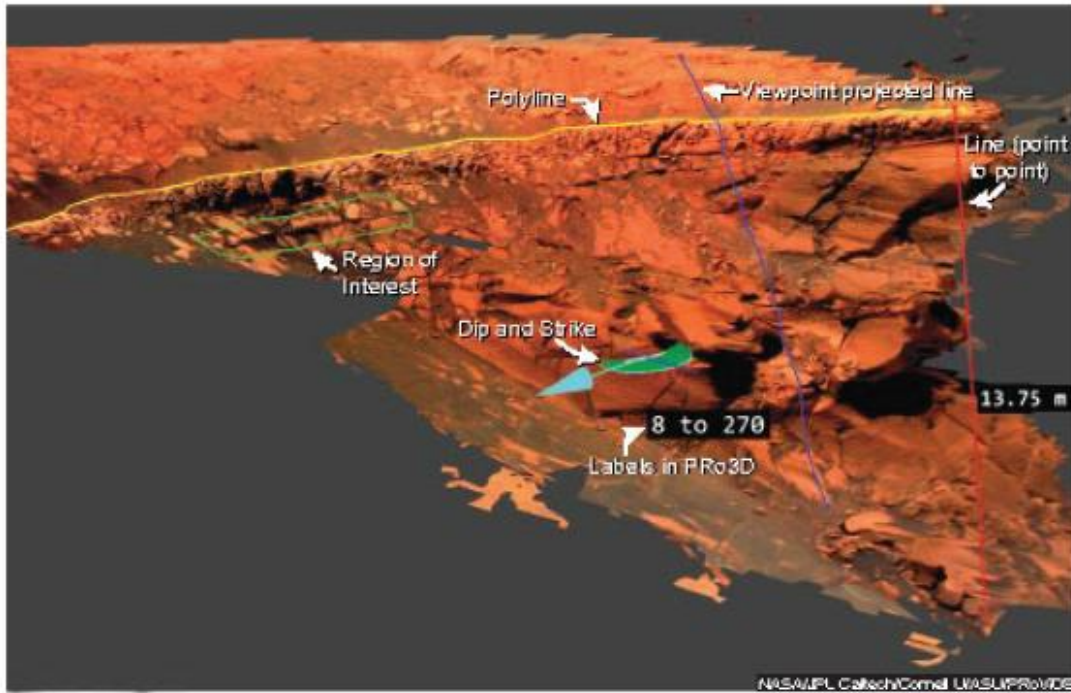
Labels visible in the figure: Polyline, Viewpoint projected line, Line (point to point), Region of Interest, Dip and Strike, 8 to 270, Labels in PRo3D, 13.75 m, NASA/JPL Caltech/Cornel UASU/PRo3D

Figure 1. (a) Summary diagram illustrating the measurement tools in PRo3D on an Ordered Point Cloud (OPC) created from MER *Opportunity* Pancam data collected on Sols 1060 and 1061 of the mission.
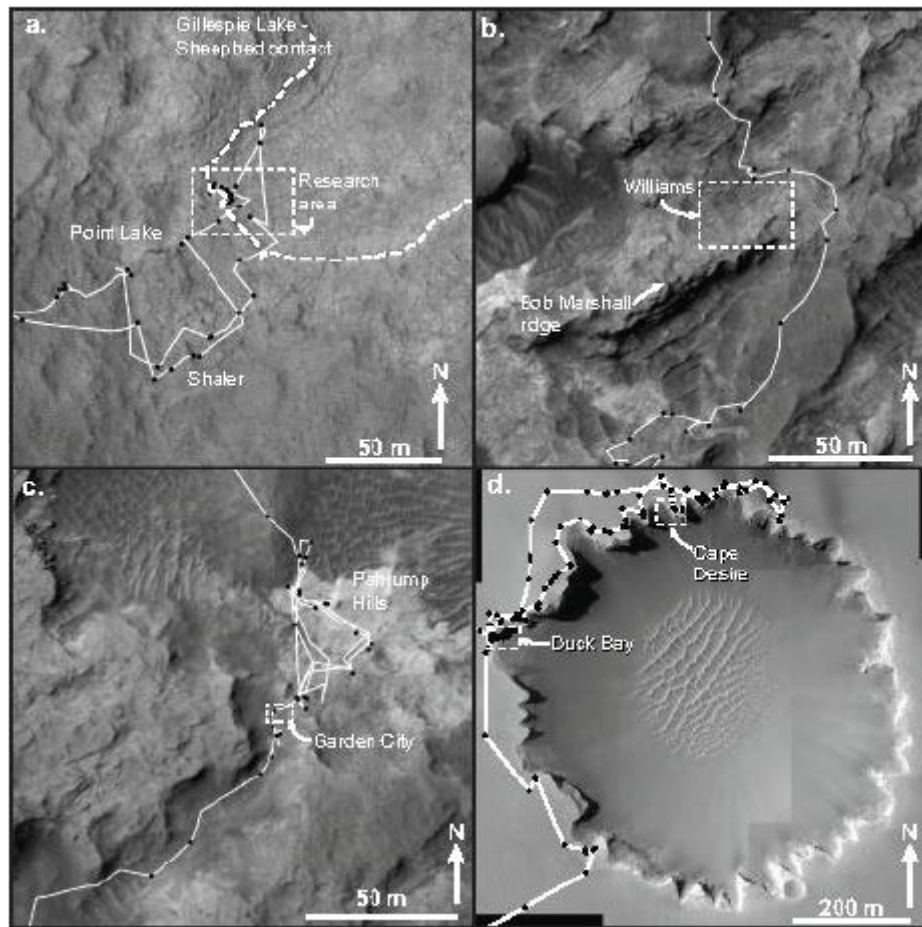
Figure 2. (a) HiRISE image of Yellowknife Bay in Gale crater, where the MSL science team investigated units mapped in Grotzinger et al., (2014). The locations at which the rover stopped to collect images and contact science data are shown. (b) HiRISE image of the Bridger Basin area, visited by the MSL rover Curiosity between Sols 1085 and 1153. The outcrops being analysed in this paper are from sols 1095 and 1148. See Banham *et al*., (2018) for a detailed description and analysis of the geology in the area. (c) HiRISE image of the MSL traverse between Sols 751 and 951. The location of the Garden City outcrop is highlighted. The fracture systems being investigated in this research are prominent in the light coloured, smooth textured unit. Analyses in this area have been included to highlight the applicability of PRo3D to structural analysis of vein and fracture systems. Image credits (a. - c.): NASA/JPL/UofA. (d) Super-resolution HiRISE image of Victoria crater which was visited by MER-B Opportunity between September 2006 and August 2008. Erosional widening has resulted in a ~ 750 m wide crater with a scalloped morphology, consisting of numerous capes and bays. Sols 952 to 1634 of the mission were spent traversing the rim of the crater, imaging rock outcrops of the Upper Burns formation and searching for a safe ingress path to enter the crater. Image credit: NASA/JPL/UofA/MSSL.
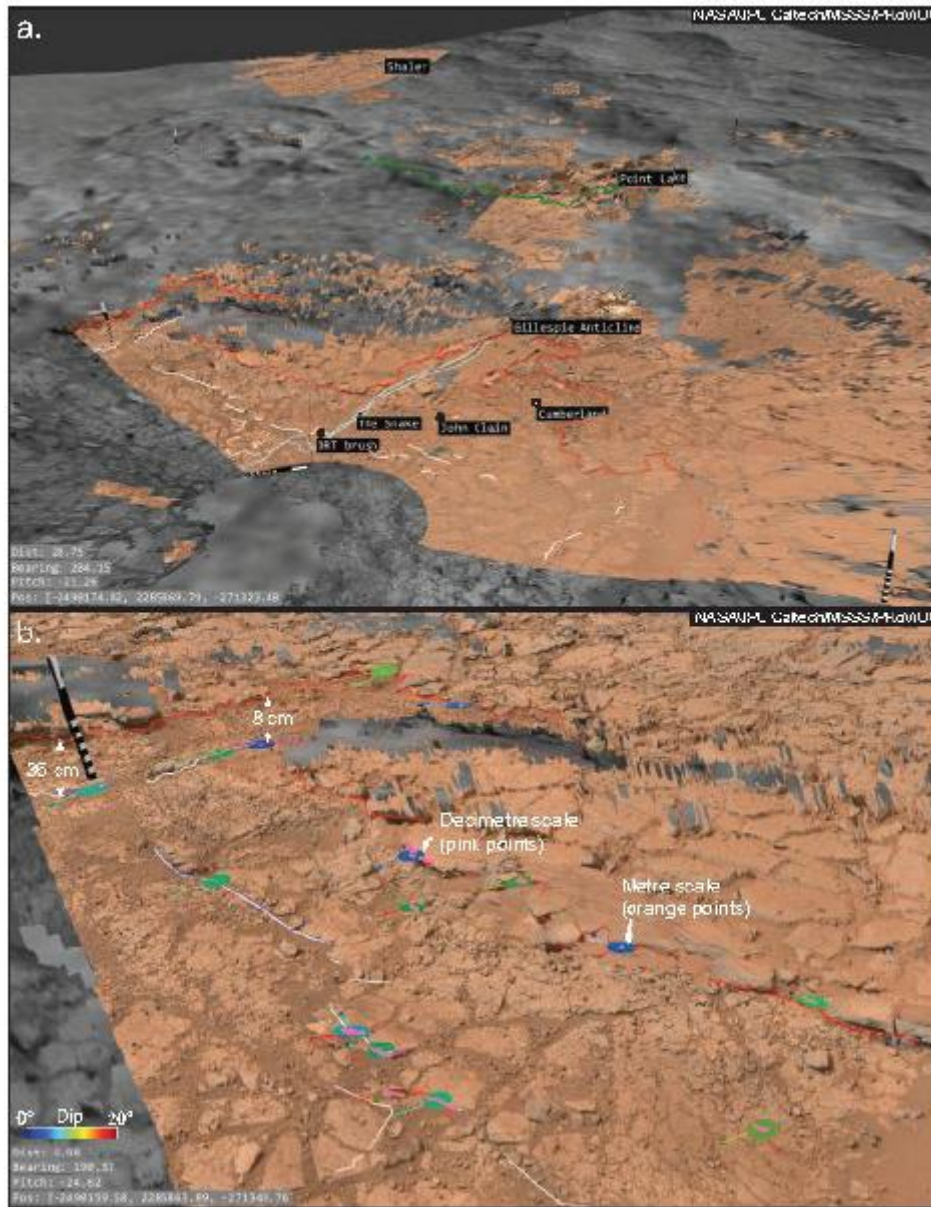
Figure 3. DOM of Yellowknife Bay created using available Mastcam and Navcam stereo data, together with a HiRISE DTM and orthoimage of the area. (a) An overview of the Yellowknife Bay area with the locations of prominent geomorphic features in the area labelled in PRo3D. The red line delineates the boundary between the basal Sheepbed mudstone and the Gillespie Lake sandstone, and the blue line at Point Lake delineates the boundary between the Gillespie Lake and Glenelg members. The locations of the John Klein and Cumberland drill sites are indicated. (b) Details of the bedding geometries wihin the Sheepbed mudsone. Dip and strike measurements have been taken to highlight the irregular geometries within the Sheepbed mudstone member. Metre scale measurements (the formative polyline is 2 - 25 m long) show the overall dip at the scale of the outcrop, and the decimetre scale measurements (10 - 70 cm long) show smaller scale variations. The irregular Sheepbed-Gillespie boundary can be seen clearly from this view position. All scale bars are 2 m.
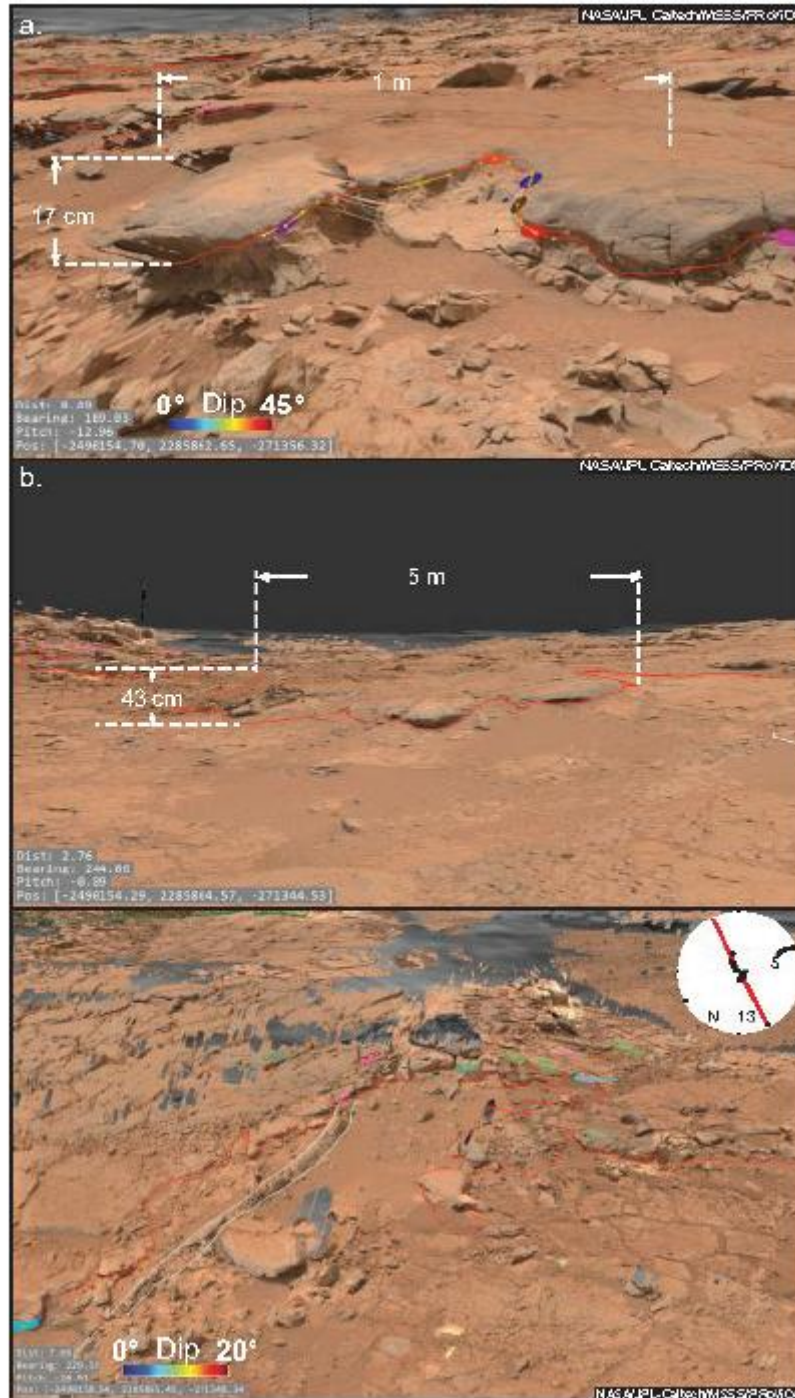
Figure 4. (a) Small sedimentary scour at the Sheepbed-Gillespie boundary, with a depth of 17 cm and a width of 1 m. Dip and strike measurements have been taken at various points around the boundary to show its irregular nature, and that it dips up to 45° approximately to the NE. (b) Larger-scale scours at the Sheepbed-Gillespie boundary, which is up to 5 m across, and 43 cm deep. (c) View along the axis of the Gillespie anticline, showing the fold geometry and the locations of dip and strike measurements. A stereonet of the poles to the measured dip and strike values in the anticline is shown inset, where "S" is the trend of the snake plotted as a line. Scale bars are 2 m.
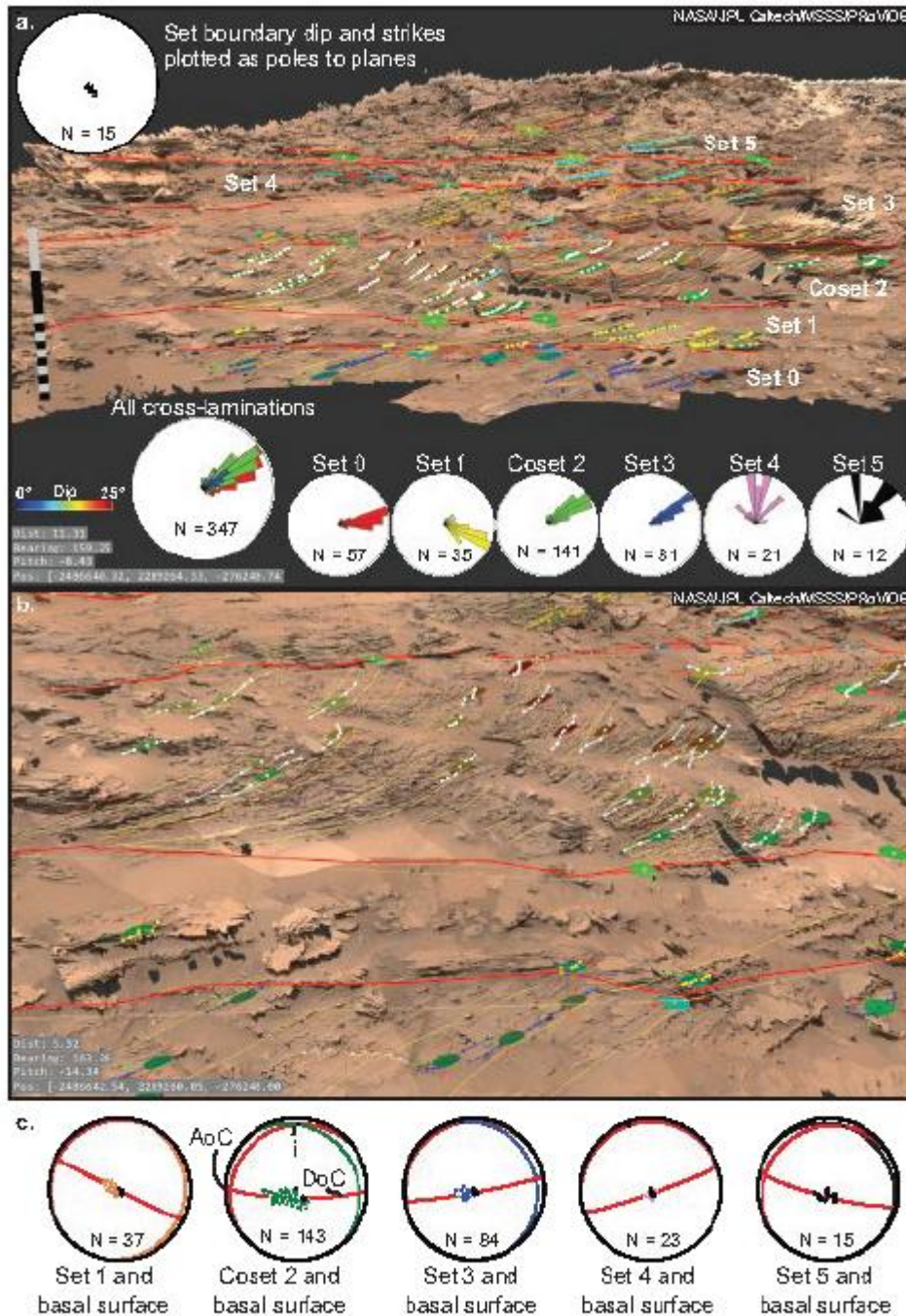
Figure 5. (a) The Williams DOM in PRo3D with interpreted set boundaries (thick red lines) and a subset of the measured dip and strikes (dotted lines with coloured disks, the red line indicated strike direction) shown to avoid obscuring the outcrop details. Lamination contacts have been mapped onto the DOM and can be seen to shallow in inclination in Sets 4 and 5. Equal distance rose diagrams with 10° bins are inset into the DOM, showing dip directions for all cross-laminations as well as divided by sets. A stereonet of the measured poles to the set boundaries is also inset in the top left. (b) Details of the asymptotic geometry of laminations in Coset 2, which is up to 2.6 m wide in outcrop and shows steep dips, up to 37° in the upper parts, and lower dips of 4° at the base. (c) Stereonets showing the poles to

laminations in Sets 1 – 5, together with the plane (same colour as poles) which describes the maximum eigenvector of these values. The maximum eigenvector for the underlying basal surface values has also been plotted to describe the mean geometry of the surface. The intersection (i) of these two planes has been calculated for each set, allowing the direction (DoC) and angle of migration (AoC) of each set to be read from each stereonet.
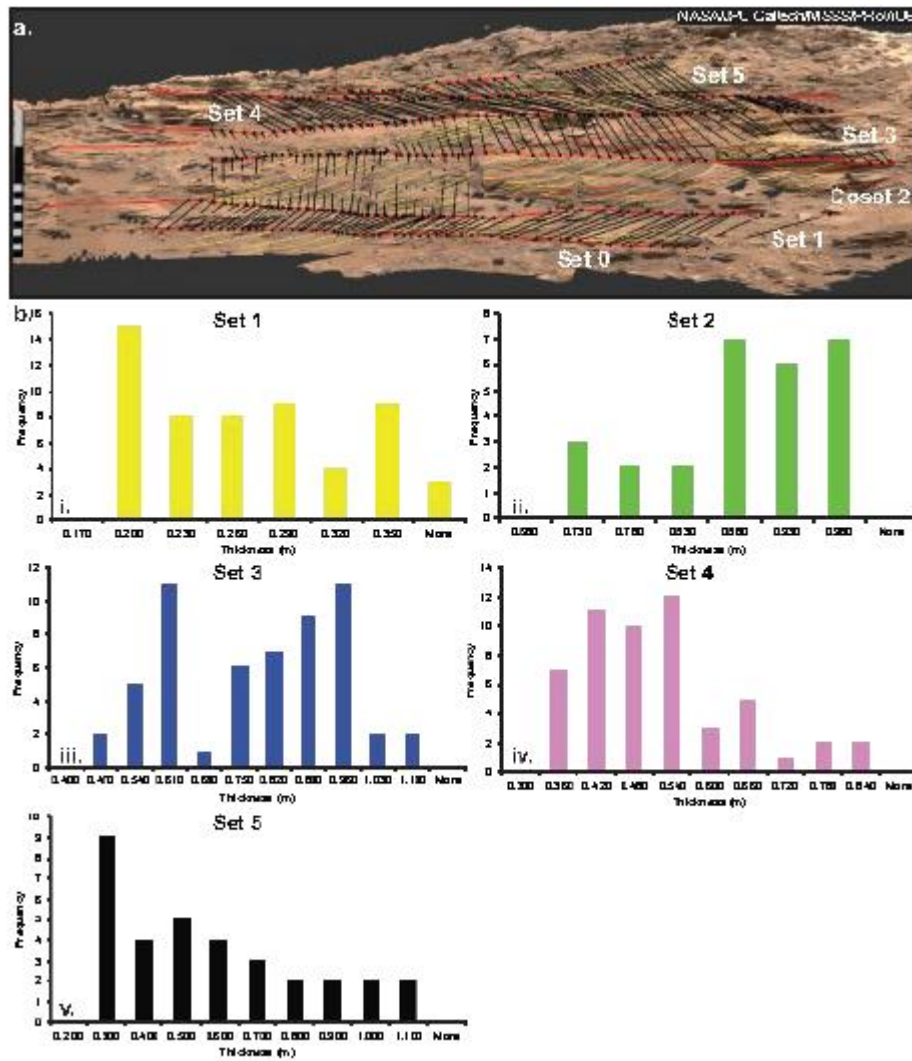
Figure 6. (a) Locations and distribution of the lines used to measure the thickness of Sets 1 – 5 from the Williams DOM. (b) Histograms of the thickness values of Sets 1 – 5.
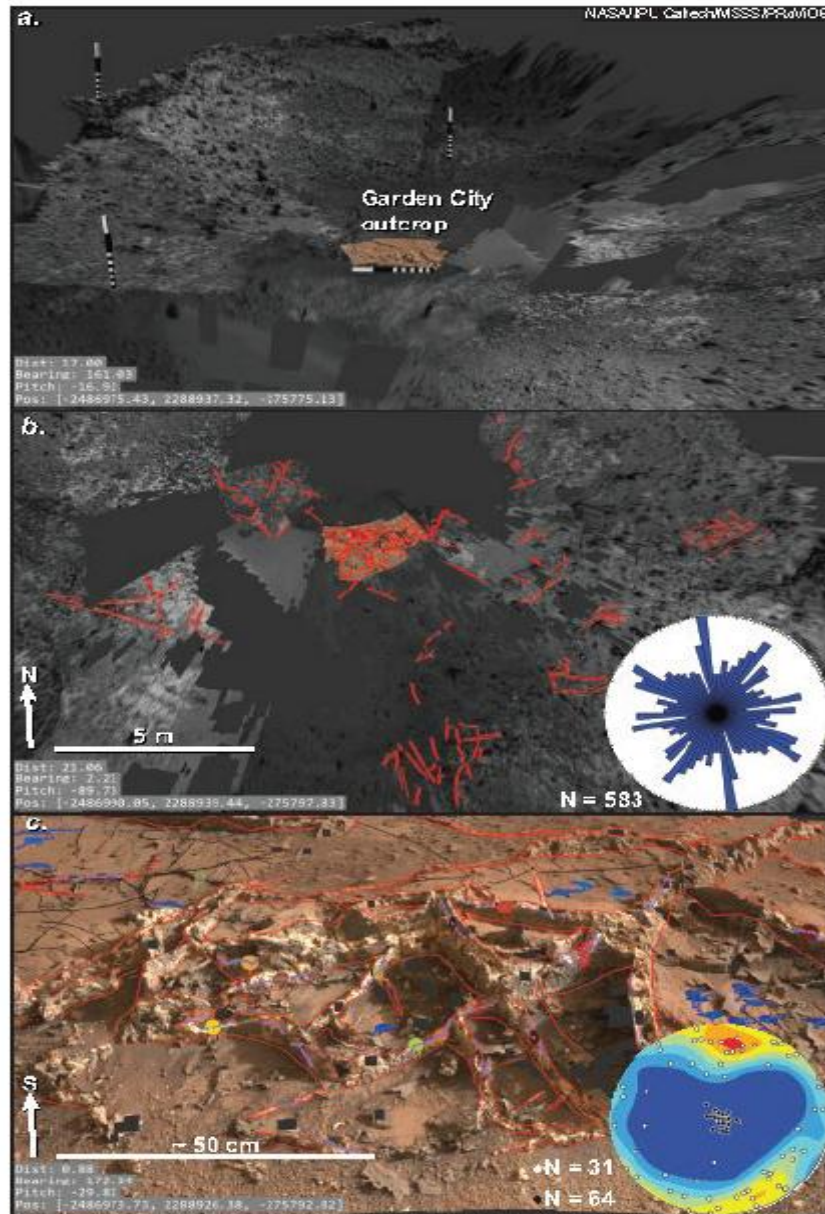
Figure 7. (a) Merged Mastcam and Navcam datasets from Sols 923 and 926 of the MSL mission, rendered in PRo3D. The location of the Garden City outcrop itself is indicated. Scale bars are 2 m. (b) Map-view of the fracture interpretation at Garden City. The boundaries of mineral-filled veins were digitised in red. An equal distance rose diagram of fracture trace orientations is inset. (c) 3D view of the Mastcam OPCs from Sols 923 and 926, showing the vein and fracture system interpretation (red and black polylines), as well as the locations of fracture dip and strike measurement (mauve lines) and bed dip and strike measurement (blue lines). A stereonet of dip and strike values from the full Garden City dataset is shown inset. Bedding is represented by the black circles, fractures by the white circles. Exponentially weighted modified Kamb contouring was used to locate maxima representing planes dipping 65° to 008° and a lesser maxima representing planes dipping 71° to 151°.
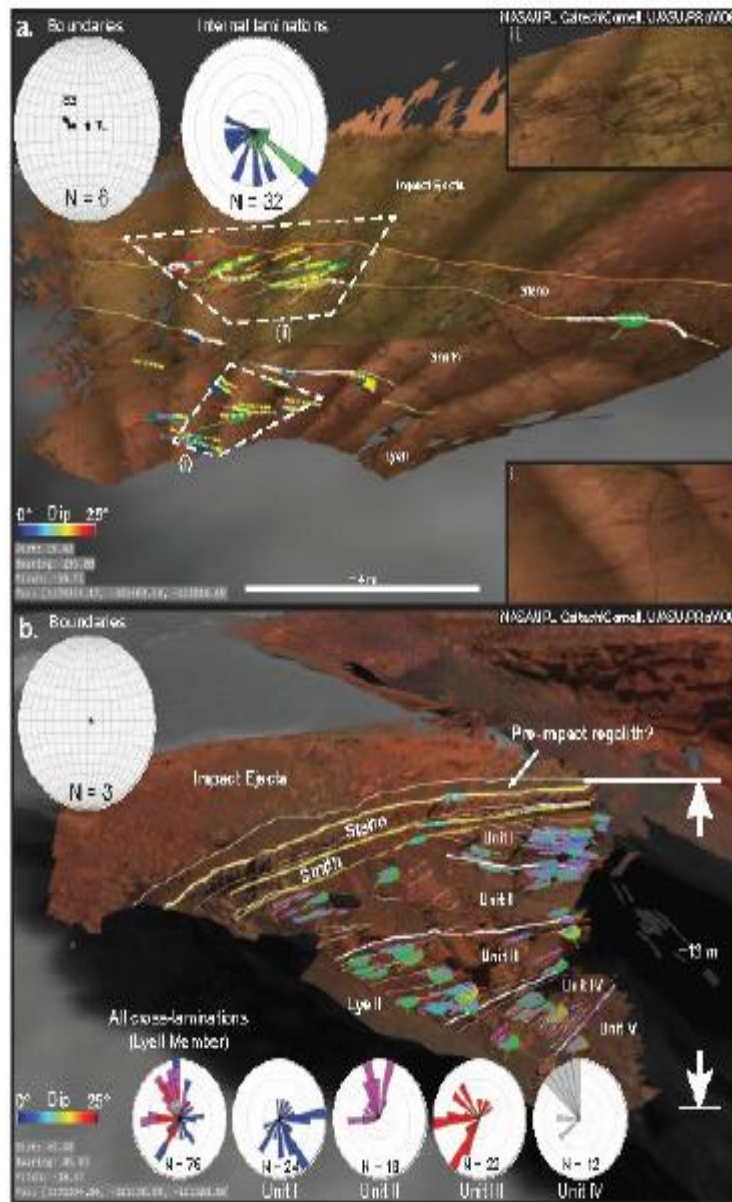
Figure 8. (a) 3D rendering of an interpreted scene of Duck Bay in PRo3D, highlighting a lower, relatively dark, pinstripe cross-laminated sandstone (Lyell unit), overlain by a diagenetically altered unit of the same material (Smith unit). There is an erosional boundary at the top of this diagenetic unit, indicated by the irregular topographic expression of the boundary, and the changes in measured dip in the finely laminated sandstone (Steno Unit), above that boundary. The boundary dip and strikes were measured along the thick white lines. Internal laminations in the Lyell and Steno are the thin yellow dotted lines. The best-fit dip planes are colour coded by dip. Inset are the stereonet indicating the attitude of the main boundaries (BS = Base Steno, TL = Top Lyell), and the laminations in the Lyell and Steno members measured at Duck Bay. (i) Blowup image of pinstripe cross-laminations in the Lyell member, the location of the image is shown in (i). (ii) Blowup image of trough cross-laminations in the Steno member. (b) Interpreted 3D scene of Cape Desire in PRo3D. The

stratigraphy has been correlated with the Duck Bay reference section. Cross-lamination patterns were mapped (thin white lines) in order to locate the bedset boundaries (thick white lines). These form 1.7 - 3.5 m thick preserved bedsets. The dip and strike of the boundaries and laminations have been calculated and show a steepening down the section. At the base of the outcrop, dip values reach up to 33°. Inset are the stereonets of the boundary dip and strike values, as well as rose diagrams of the dip directions measured at Cape Desire, showing all values, as well as the individual values for Units I-IV. Dip and strike values were not measured in Unit V due to a lack of 3D exposure of laminations there.